Finite Elements in Analysis and Design 204 (2022) 103741

Contents lists available at ScienceDirect

Finite Elements in Analysis & Design

journal homepage: www.elsevier.com/locate/finel

Locking-free 6-noded triangular shell elements based on hierarchic optimisation

Y. Liang [a,b], B.A. Izzuddin [c,*]

[a] Department of Civil and Environmental Engineering, Imperial College London, SW7 2AZ, United Kingdom
[b] School of Engineering, University of Glasgow, G12 8QQ, United Kingdom
[c] Professor of Computational Structural Mechanics, Department of Civil and Environmental Engineering, Imperial College London, SW7 2AZ, United Kingdom

ARTICLE INFO

Keywords:
Locking
Triangular shell element
Hierarchic optimisation
Large displacement analysis

ABSTRACT

Conforming lower-order shell elements based on Reissner-Mindlin plate theory generally exhibit an over-stiff response under loading, typically manifested through various forms of locking. A recently developed hierarchic optimisation approach addresses locking by enriching the conforming strains with hierarchic strain terms towards an objective 'smoother' strain distribution afforded by the element, which has proven to be effective in relieving shear, membrane and distortion locking in 9-noded quadrilateral shell elements. Nevertheless, in some practical structural problems that involve complex geometry, triangular shell elements are required to avoid a highly distorted mesh of quadrilateral elements. This paper presents a family of 6-noded Reissner-Mindlin triangular shell elements based on the hierarchic optimisation approach. The proposed curved triangular shell elements not only effectively alleviate inaccuracies arising from locking, but also embrace the desirable characteristics of spatial isotropy and insensitivity to element distortion. The family of 6-noded triangular elements have been incorporated within a co-rotational framework to allow large displacement analysis of thin to moderately thick plates and shells. Several numerical examples are finally presented to demonstrate the effectiveness and accuracy of the proposed 6-noded shell element formulation as well as its superior locking-free performance compared to existing shell elements.

1. Introduction

Displacement-based low-order plate and shell elements usually suffer from locking phenomena, where the element exhibits an over-stiff response particularly for very thin plate and shell applications, owing principally to the inability of the element to capture the low-order deformation modes. The severity of locking is dependent on several parameters, including the type of structural analysis problem, the theory underlying the associated mathematical model, and the element shape and order. Since quadrilateral shell elements are predominantly employed for modelling regular structures in many engineering applications, numerous research efforts have been devoted to establishing optimal locking-free quadrilateral elements [1–13]. In some practical structural problems that involve complex geometry, however, triangular finite elements are inevitably used so as to avoid highly distorted meshes of quadrilateral elements. A few studies have been conducted to improve the performance of low-order triangular plate and shell elements by using various locking-elimination approaches, including reduced/selective integration methods [3,14], enhanced displacement methods [4,15,16], and assumed strain methods [8,17–22]. Even so, the fewer strain modes afforded by the triangular elements and the difficulty of fulfilling 'spatial isotropy' [18], in comparison with the quadrilateral counterparts, present barriers to the development of optimal locking-free triangular elements. Furthermore, triangular plate and shell elements are mainly used in problems with a complex geometric configuration, hence requiring these elements to be insensitive to irregularity in the element shape. Therefore, an effective triangular shell element needs to: (i) provide an optimal relief of locking, (ii) preserve the isotropic characteristic, and (iii) allow element distortion.

A hierarchic optimisation approach [13] has been recently proposed by the authors for nonlinear shell finite elements, which is an assumed strain method that not only addresses shear and membrane locking but also alleviates locking due to element distortion. This approach introduces two sets of strain modes: (i) *objective* strain modes, defined in the physical coordinate system and serving as the target strain modes, and (ii) *hierarchic* correcting strain modes, defined in the natural

* Corresponding author.
E-mail address: b.izzuddin@imperial.ac.uk (B.A. Izzuddin).

https://doi.org/10.1016/j.finel.2022.103741
Received 29 October 2021; Received in revised form 31 January 2022; Accepted 5 February 2022
Available online 4 March 2022

coordinate system for correcting the conforming strains. Accordingly, an assumed strain distribution within an element may be expressed as a linear combination of either (i) the *objective* strain modes, or (ii) the *corrective* strain modes that comprise both the conforming and the hierarchic correcting strain modes. By performing mathematical optimisation on the difference between the objective strains and the corrective strains over the element domain, the values of the corresponding strain parameters can be determined prior to the start of nonlinear analysis, while maintaining the same degrees of freedom (DOF) of the underlying conforming element. With the successful application of this approach to a 9-noded quadrilateral shell element [13], the present paper aims to extend its application to a 6-noded triangular shell element, which is expected to address the various forms of locking, preserve element isotropy and tolerate element distortion.

In the following sections, the hierarchic optimisation approach is firstly outlined, followed by an elaboration of its application to the local formulation of a family of 6-noded Reissner-Mindlin shell elements. The incorporation of the various local formulations into a co-rotational coordinate system, based on a zero-macrospin definition of the local coordinate system [23], is subsequently presented, which enables the application of the proposed elements in geometrically nonlinear analysis. The performance of the optimised 6-noded elements is finally assessed through several benchmark numerical examples, with the efficiency and relative accuracy compared with other previously developed triangular shell elements.

2. Hierarchic optimisation approach

The locking phenomena in conforming finite elements is generally characterised by the degraded approximation of various strains over the element domain, principally owing to polluting higher-order strains. The hierarchic optimisation approach [13] overcomes locking by reconstructing a smoother strain distribution within the element domain, which can be regarded as a threefold approach. Firstly, a set of smooth strain modes $\boldsymbol{\Psi}_o$ are defined on the physical element configuration, which form the modal basis for a so-called *objective* 'smoothed' strain distribution $\boldsymbol{\varepsilon}_o$. Secondly, hierarchic correcting strains $\boldsymbol{\varepsilon}_h$, which comprise various higher-order strain modes $\boldsymbol{\Psi}_h$ beyond those employed in the conforming isoparametric element formulation, are defined to enrich the conforming strains $\boldsymbol{\varepsilon}$, with the resulting strain combination ($\boldsymbol{\varepsilon} + \boldsymbol{\varepsilon}_h$) denoted as the *corrective* strains. Finally, mathematical optimisation is performed at the element level to enforce a best fit between the *objective* strain distribution $\boldsymbol{\varepsilon}_o$ and the *corrective* strain distribution ($\boldsymbol{\varepsilon} + \boldsymbol{\varepsilon}_h$) within the element domain, where the strain parameters associated with both the objective and hierarchic strain modes can be determined. Thus, through a strain transformation process, the conforming strains are replaced by either *objective* strains or *corrective* strains, leading to two respective families of variant elements as elaborated later.

The hierarchic and objective strains are defined as follows:

$$\boldsymbol{\varepsilon}_h = \boldsymbol{\Psi}_h \boldsymbol{\alpha}_h, \quad \boldsymbol{\varepsilon}_o = \boldsymbol{\Psi}_o \boldsymbol{\alpha}_o \tag{1}$$

where $\boldsymbol{\Psi}_h$ and $\boldsymbol{\Psi}_o$ are the hierarchic and objective strain modes, respectively, while $\boldsymbol{\alpha}_h$ and $\boldsymbol{\alpha}_o$ are the respective associated strain parameters.

The employment of mathematical optimisation leads to a minimisation of the difference between the *corrective* strains ($\boldsymbol{\varepsilon} + \boldsymbol{\varepsilon}_h$) and the *objective* strains $\boldsymbol{\varepsilon}_o$. Considering the target of optimisation to be a functional integrating the square of this difference over the element domain, the strain parameters $\boldsymbol{\alpha}_h$ and $\boldsymbol{\alpha}_o$ can be obtained for a given set of conforming strains $\boldsymbol{\varepsilon}$ by solving the following linear system of equations at the level of an individual element [13]:

$$\left(\int_{\Omega^e} \left[\begin{array}{c|c} \boldsymbol{\Psi}_h^{\mathrm{T}} \boldsymbol{\Psi}_h & -\boldsymbol{\Psi}_h^{\mathrm{T}} \boldsymbol{\Psi}_o \\ \hline -\boldsymbol{\Psi}_o^{\mathrm{T}} \boldsymbol{\Psi}_h & \boldsymbol{\Psi}_o^{\mathrm{T}} \boldsymbol{\Psi}_o \end{array} \right] \mathrm{d}\Omega^e \right) \left\{ \begin{array}{c} \boldsymbol{\alpha}_h \\ \hline \boldsymbol{\alpha}_o \end{array} \right\} = \int_{\Omega^e} \left[\begin{array}{c} -\boldsymbol{\Psi}_h^{\mathrm{T}} \\ \hline \boldsymbol{\Psi}_o^{\mathrm{T}} \end{array} \right] \boldsymbol{\varepsilon} \, \mathrm{d}\Omega^e \tag{2}$$

in which Ω^e is the physical element domain.

For isoparametric elements, Gaussian quadrature is employed to numerically integrate Eq. (2), resulting in $\boldsymbol{\alpha}_h$ and $\boldsymbol{\alpha}_o$ being related to the strains $\boldsymbol{\varepsilon}_{(i)}$ at the Gauss points as follows:

$$\boldsymbol{\alpha}_h = \boldsymbol{\Gamma}_h \left\{ \begin{array}{c} \boldsymbol{\varepsilon}_{(1)} \\ \vdots \\ \boldsymbol{\varepsilon}_{(i)} \\ \vdots \end{array} \right\}, \quad \boldsymbol{\alpha}_o = \boldsymbol{\Gamma}_o \left\{ \begin{array}{c} \boldsymbol{\varepsilon}_{(1)} \\ \vdots \\ \boldsymbol{\varepsilon}_{(i)} \\ \vdots \end{array} \right\} \tag{3}$$

in which the subscript (i) represents the Gauss point number.

The determination of the strain parameters $\boldsymbol{\alpha}_h$ and $\boldsymbol{\alpha}_o$ from the conforming strains $\boldsymbol{\varepsilon}$ without reference to the element nodal displacement parameters preserves the computational efficiency, particularly for nonlinear strain-displacement relationships, and the conforming strains are accordingly enhanced with hierarchic higher-order strains towards the objective strains. The enhanced strains can be expressed in either the *corrective* or the *objective* form, where the difference between the two alternative approaches reduces with either the hierarchic order or mesh refinement [13]:

$$\widetilde{\boldsymbol{\varepsilon}} = \boldsymbol{\varepsilon} + \boldsymbol{\Psi}_h \boldsymbol{\alpha}_h \quad \text{(Corrective)} \tag{4}$$

$$\widehat{\boldsymbol{\varepsilon}} = \boldsymbol{\Psi}_o \boldsymbol{\alpha}_o \quad \text{(Objective)} \tag{5}$$

Considering the above, an assumed strain formulation can be derived, with the values of the assumed strains evaluated at the Gauss points as follows, depending on the alternative approach:

$$\left\{ \begin{array}{c} \widetilde{\boldsymbol{\varepsilon}}_{(1)} \\ \vdots \\ \widetilde{\boldsymbol{\varepsilon}}_{(i)} \\ \vdots \end{array} \right\} = \widetilde{\mathbf{T}} \left\{ \begin{array}{c} \boldsymbol{\varepsilon}_{(1)} \\ \vdots \\ \boldsymbol{\varepsilon}_{(i)} \\ \vdots \end{array} \right\}, \quad \widetilde{\mathbf{T}} = \mathbf{I} + \left[\begin{array}{c} \boldsymbol{\Psi}_{h(1)} \\ \vdots \\ \boldsymbol{\Psi}_{h(i)} \\ \vdots \end{array} \right] \boldsymbol{\Gamma}_h \quad \text{(Corrective)} \tag{6}$$

$$\left\{ \begin{array}{c} \widehat{\boldsymbol{\varepsilon}}_{(1)} \\ \vdots \\ \widehat{\boldsymbol{\varepsilon}}_{(i)} \\ \vdots \end{array} \right\} = \widehat{\mathbf{T}} \left\{ \begin{array}{c} \boldsymbol{\varepsilon}_{(1)} \\ \vdots \\ \boldsymbol{\varepsilon}_{(i)} \\ \vdots \end{array} \right\}, \quad \widehat{\mathbf{T}} = \left[\begin{array}{c} \boldsymbol{\Psi}_{o(1)} \\ \vdots \\ \boldsymbol{\Psi}_{o(i)} \\ \vdots \end{array} \right] \boldsymbol{\Gamma}_o \quad \text{(Objective)} \tag{7}$$

in which $\widetilde{\mathbf{T}}$ and $\widehat{\mathbf{T}}$ are transformation matrices from conforming strains to corrective strains and objective strains, respectively, at the Gauss points.

The above alternative approaches correspond to an assumed strain formulation, though the assumed strains are the result of optimisation towards a specific target strain distribution afforded by the original conforming DOFs, as demonstrated in Ref. [13]. For geometrically linear elements, which employ a first-order strain-displacement relationship, the assumed strains $\widetilde{\boldsymbol{\varepsilon}}$ or $\widehat{\boldsymbol{\varepsilon}}$ can be directly related to the original DOFs via a respective strain operator $\widetilde{\mathbf{B}}$ or $\widehat{\mathbf{B}}$, since $\boldsymbol{\varepsilon}$ is readily related to such DOFs through the conventional conforming $\mathbf{B}$ matrix. For geometrically nonlinear elements, however, it is more effective to determine the conforming strains and then transform these to assumed strains according to Eq. (6) or Eq. (7).

Unlike other enhanced assumed strain approaches [5,6], the hierarchic optimisation approach results in two variant element families, depending on whether the corrective (C) or objective (O) fields are adopted for the assumed strains. Furthermore, while the hierarchic correcting strain field $\boldsymbol{\varepsilon}_h$ resembles the enhanced assumed strain in previous approaches, its approximation order is not capped to a prescribed distribution but can attain any hierarchic order m. On the other hand, the additionally introduced objective strain field $\boldsymbol{\varepsilon}_o$ is similar conceptually to an assumed strain field based on sampling at selected locations [9–12], but it is different in two ways [13]: (i) it utilises a polynomial basis in physical Cartesian coordinates which effectively addresses distortion locking in isoparametric element formulations with irregular element configuration; (ii) it is recovered via an optimisation process that considers the conforming strains $\boldsymbol{\varepsilon}$ over the whole element

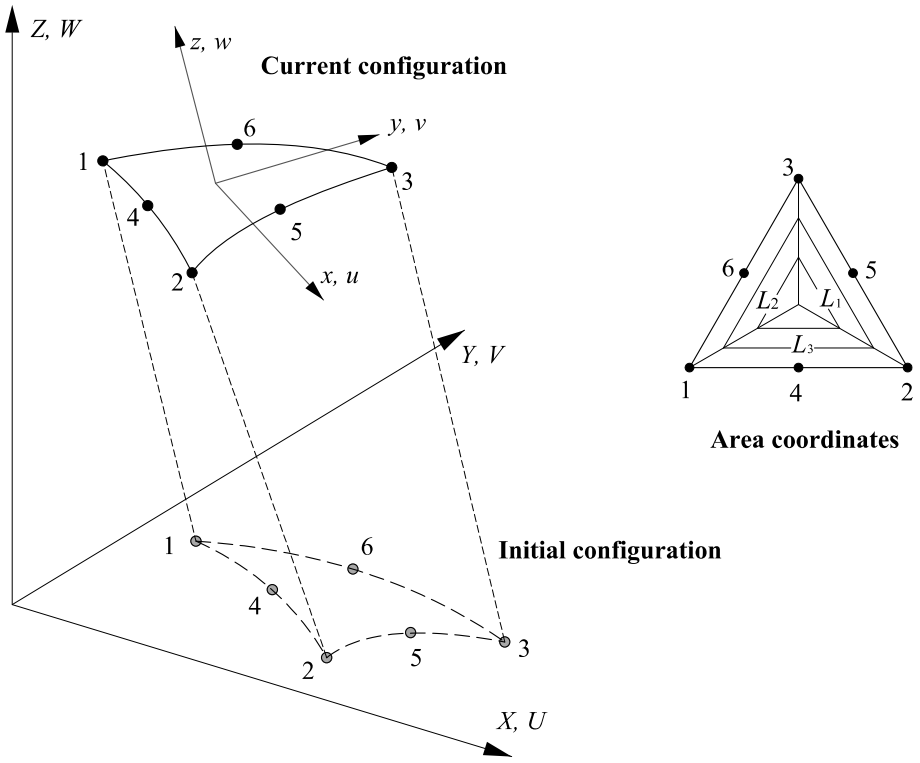

a. Global, local and area coordinates for 6-noded shell element.

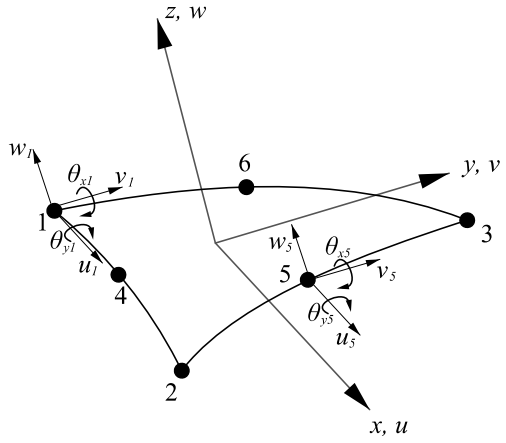

b. Local nodal DOFs for 6-noded shell element.

Fig. 1. Coordinate systems and nodal DOFs for 6-noded shell element.

domain rather than at a fixed number of sampling points. The following section presents the local formulation of the two variant families of the 6-noded hierarchically optimised element, denoted by acronyms H*m*C6 and H*m*O6, respectively based on corrective and objective strain fields, where m is the hierarchic correction order used for ε_h.

3. Optimised 6-noded triangular element in local system

In this section, the hierarchic optimisation approach is employed to address the locking issue in the local formulation of a 6-noded shell element based on the Reissner-Mindlin hypothesis. Fig. 1 shows the global Cartesian, the local Cartesian, and the area coordinate systems used for the 6-noded shell element undergoing large displacements, with the associated coordinate systems denoted by (X, Y, Z), (x, y, z), and (L_1, L_2, L_3), respectively. A local co-rotational system is used for the shell element, so that throughout the deformation history the xy plane of the local system is always defined by the three corner nodes 1, 2 and 3, while the local z-axis is normal to the xy plane.

In the following sub-sections, the local kinematics of the 6-noded Reissner-Mindlin shell element are firstly presented; subsequently,

hierarchic optimisation of this conforming element is elaborated, and adjustments are made to the optimisation approach to enable the preservation of spatial isotropy for triangular element applications.

3.1. Local conforming formulation of 6-noded triangular shell element

In the local formulation, each node corresponds to 5 DOFs, including 3 local translational DOFs and 2 local rotational DOFs, as illustrated in Fig. 1 b for local nodal DOFs at nodes 1 and 5. For an isoparametric 6-noded shell element, the local element geometry and displacement fields can be interpolated using shape functions N_i that are expressed in terms of area coordinates (L_1, L_2, L_3):

$$\mathbf{x} = \begin{Bmatrix} x \\ y \\ z \end{Bmatrix} = \sum_{i=1}^{6} N_i(L_1, L_2, L_3)\mathbf{x}_i \tag{8}$$

$$\mathbf{t} = \begin{Bmatrix} u \\ v \\ w \end{Bmatrix} = \sum_{i=1}^{6} N_i(L_1, L_2, L_3)\mathbf{t}_i, \quad \bar{\mathbf{r}} = \begin{Bmatrix} \theta_x \\ \theta_y \end{Bmatrix} = \sum_{i=1}^{6} N_i(L_1, L_2, L_3)\bar{\mathbf{r}}_i \tag{9}$$

where $\mathbf{x}_i = \langle\, x_i \quad y_i \quad z_i \,\rangle^{\mathrm{T}}$ are local nodal coordinates of node i in the initial configuration; $\mathbf{t}_i = \langle\, u_i \quad v_i \quad w_i \,\rangle^{\mathrm{T}}$ are local nodal translations of node i; $\bar{\mathbf{r}}_i = \langle\, \theta_{xi} \quad \theta_{yi} \,\rangle^{\mathrm{T}}$ are the local nodal rotations of node i (θ_{xi} is the nodal rotation about the y-axis and θ_{yi} is the nodal rotation about the negative x-axis); and the shape functions N_i are expressed in terms of area coordinates as follows:

$$N_i = L_i(2L_i - 1), \quad N_{i+3} = 4L_iL_{i+} \quad (i = 1 \to 3) \tag{10}$$

in which the area coordinate L_i equals 1 at node i, and reduces linearly to 0 at edge i_-–i_+; $i_+ = \mathrm{mod}(i, 3) + 1$; and $i_- = \mathrm{mod}(i_+, 3) + 1$. The area coordinates ($L_1$, L_2, L_3) are related to natural coordinates (ξ, η) by setting $L_1 = 1 - \xi - \eta$, $L_2 = \xi$, and $L_3 = \eta$, where $\xi,\ \eta \in [0, 1]$.

The strain state of the shell element is fully determined by membrane strains $\boldsymbol{\varepsilon}^m$, generalised bending strains $\boldsymbol{\varepsilon}^b$, and transverse shear strains $\boldsymbol{\varepsilon}^s$ as follows:

$$\boldsymbol{\varepsilon}^m = \begin{Bmatrix} \varepsilon_x \\ \varepsilon_y \\ \gamma_{xy} \end{Bmatrix} = \begin{Bmatrix} \dfrac{\partial u}{\partial x} \\ \dfrac{\partial v}{\partial y} \\ \dfrac{\partial u}{\partial y} + \dfrac{\partial v}{\partial x} \end{Bmatrix} + \begin{Bmatrix} \dfrac{1}{2}\left(\dfrac{\partial z}{\partial x} + \dfrac{\partial w}{\partial x}\right)^2 - \dfrac{1}{2}\left(\dfrac{\partial z}{\partial x}\right)^2 \\ \dfrac{1}{2}\left(\dfrac{\partial z}{\partial y} + \dfrac{\partial w}{\partial y}\right)^2 - \dfrac{1}{2}\left(\dfrac{\partial z}{\partial y}\right)^2 \\ \left(\dfrac{\partial z}{\partial x} + \dfrac{\partial w}{\partial x}\right)\left(\dfrac{\partial z}{\partial y} + \dfrac{\partial w}{\partial y}\right) - \left(\dfrac{\partial z}{\partial x}\right)\left(\dfrac{\partial z}{\partial y}\right) \end{Bmatrix} \tag{11a}$$

$$\boldsymbol{\varepsilon}^b = \begin{Bmatrix} \kappa_x \\ \kappa_y \\ \kappa_{xy} \end{Bmatrix} = \begin{Bmatrix} \dfrac{\partial \theta_x}{\partial x} \\ \dfrac{\partial \theta_y}{\partial y} \\ \dfrac{\partial \theta_x}{\partial y} + \dfrac{\partial \theta_y}{\partial x} \end{Bmatrix} \tag{11b}$$

$$\boldsymbol{\varepsilon}^s = \begin{Bmatrix} \gamma_{xz} \\ \gamma_{yz} \end{Bmatrix} = \begin{Bmatrix} \theta_x + \dfrac{\partial w}{\partial x} \\ \theta_y + \dfrac{\partial w}{\partial y} \end{Bmatrix} \tag{11c}$$

It is worth noting that local geometric nonlinearity is allowed for through quadratic approximation of the membrane strains, while the influence of large displacements is accounted for through transformations between the local co-rotational system and the global system [23], as elaborated in Section 4.

3.2. Objective strain modes

As mentioned in Section 2, the locking issue results principally from the inability of an element to generate some of the low-order strain modes. In other words, a locking-free finite element should be capable of generating all low-order strain modes that are afforded by the element. A full set of such strain modes for the 6-noded shell element is given in this sub-section, denoted as the objective strain modes. Importantly, the objective strain modes are defined in terms of the local physical Cartesian coordinates (x, y), rather than the natural coordinates, which inherently takes into account the actual element geometry, thereby providing a natural treatment of distortion locking. It is also important to note that the number of objective strain modes equals the number of strain-inducing displacement modes afforded by the 6-noded triangular element, hence ensuring that no spurious mechanism is induced. The complete set of low-order strain modes specific to the 6-noded triangular shell element is given as follows.

The planar displacements (u, v) for the 6-noded shell element can generate three rigid body modes and nine membrane strain-inducing modes. Therefore, nine low-order objective planar strain modes $\boldsymbol{\Psi}_o^m$ can be afforded by the element as follows:

$$\boldsymbol{\Psi}_o^m = \begin{bmatrix} \dfrac{\partial}{\partial x} & 0 \\ 0 & \dfrac{\partial}{\partial y} \\ \dfrac{\partial}{\partial y} & \dfrac{\partial}{\partial x} \end{bmatrix} \boldsymbol{\Phi}_o^m \tag{12}$$

where $\boldsymbol{\Phi}_o^m$ are objective planar strain-inducing modes from Pascal's triangle, given by:

$$\boldsymbol{\Phi}_o^m = \left[\begin{array}{ccc|c|c} x & y & 0 & \boldsymbol{\Phi}_o^2 & \mathbf{0} \\ 0 & x & y & \mathbf{0} & \boldsymbol{\Phi}_o^2 \end{array}\right], \quad \boldsymbol{\Phi}_o^2 = \left\langle x^2 \quad xy \quad y^2 \right\rangle \tag{13}$$

The transverse displacement field (w) for the 6-noded shell element provides one rigid body mode and five transverse shear strain modes. Accordingly, five low-order objective transverse shear strain modes $\boldsymbol{\Psi}_o^{s,z}$ can be provided by the element, which, together with the associated transverse shear strain-inducing modes $\boldsymbol{\Phi}_o^{s,z}$, are given by:

$$\boldsymbol{\Psi}_o^{s,z} = \begin{Bmatrix} \dfrac{\partial}{\partial x} \\ \dfrac{\partial}{\partial y} \end{Bmatrix} \boldsymbol{\Phi}_o^{s,z}, \quad \boldsymbol{\Phi}_o^{s,z} = \langle\, x \quad y \quad x^2 \quad xy \quad y^2 \,\rangle \tag{14}$$

The rotational fields $(\theta_x,\ \theta_y)$ of the 6-noded shell element afford nine curvature-inducing modes, with the objective curvature-inducing displacement modes $\boldsymbol{\Phi}_o^b$ and the corresponding bending strain modes $\boldsymbol{\Psi}_o^b$ being the same as the planar strain counterparts:

$$\boldsymbol{\Phi}_o^b = \boldsymbol{\Phi}_o^m, \quad \boldsymbol{\Psi}_o^b = \boldsymbol{\Psi}_o^m \tag{15}$$

With four rigid body modes already accounted for in relation to the planar and transverse displacement fields, the remaining two rigid body modes are generated by combining the two constant rotation modes with a linear distribution of the transverse displacement. This leaves one rotational mode that generates no curvatures but a linear transverse shear strain mode $\boldsymbol{\Psi}_o^{s,\theta} = \langle -y, x \rangle^{\mathrm{T}}$, which is not included in Eq. (14). Therefore, a complete objective set of transverse shear strain modes is given by:

$$\boldsymbol{\Psi}_o^s = \left[\boldsymbol{\Psi}_o^{s,z} \,\middle|\, \boldsymbol{\Psi}_o^{s,\theta}\right] \tag{16}$$

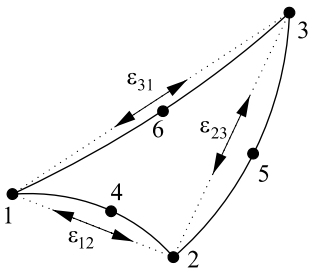

Fig. 2. Three edge-based strains of 6-noded triangular shell element.

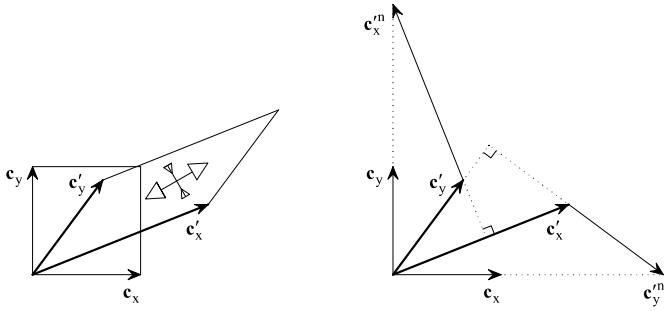

Fig. 3. Influence of a uniform 'stretch' operation on unit square area [23].

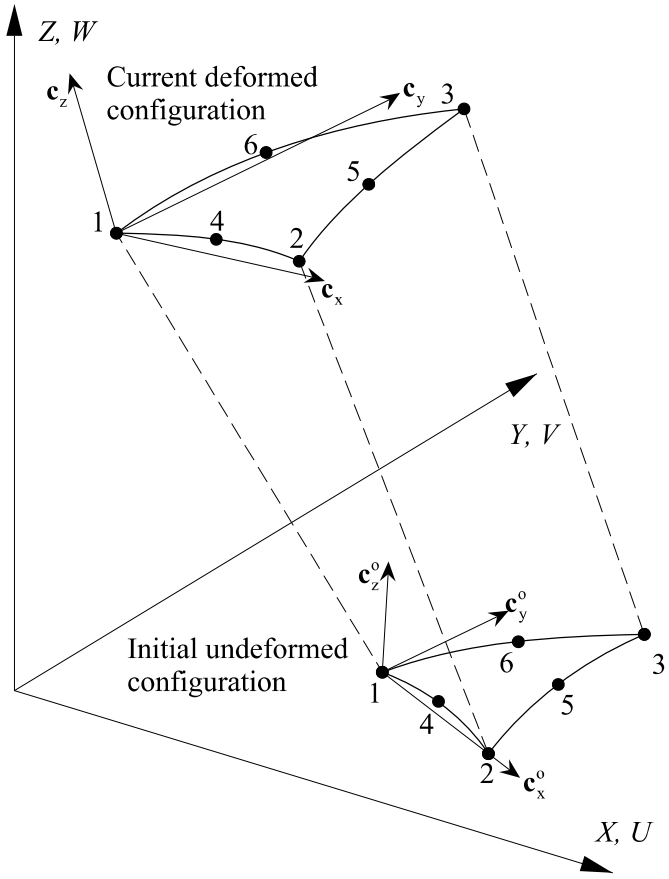

Fig. 4. Zero-macrospin local co-rotational system for 6-noded triangular element.

Table 1
Variants of 6-noded shell elements considered.

Acronym key	Strain field	Hierarchic order	Sampling Gauss points
CNF6	Conforming	–	13
H2O6	Assumed, Objective	–	13
H3O6	Assumed, Objective	3	13
H4O6	Assumed, Objective	4	16
H3C6	Assumed, Corrective	3	13
H4C6	Assumed, Corrective	4	16
MITC6*	Assumed, MITC6*	–	13

In summary, 24 objective strain modes are defined for the 6-noded triangular shell element, including 9 membrane strain modes $\boldsymbol{\Psi}_o^m$, 9 curvature modes $\boldsymbol{\Psi}_o^b$ and 6 transverse shear strain modes $\boldsymbol{\Psi}_o^s$, which ensures the correct rank of the element stiffness matrix. These objective strain modes are employed in the optimisation approach for addressing shear, membrane and distortion locking of the conforming 6-noded shell element, as presented in Section 3.3. Note that for isoparametric elements such as the considered 6-noded shell element, the objective strain modes $\boldsymbol{\Psi}_o^m$, $\boldsymbol{\Psi}_o^b$ and $\boldsymbol{\Psi}_o^s$ are initially defined in terms of physical Cartesian coordinates (x, y) for an inherent treatment of locking due to element distortion; later on, when hierarchic optimisation of the strains is conducted, these objective strain modes will be expressed in terms of the natural coordinates (ξ, η) for performing numerical integration [13].

3.3. Elimination of locking

As evident from Eq. (11c), for an arbitrary bending mode, the rotational displacements $(\theta_x,\ \theta_y)$ in a conforming 6-noded Reissner-Mindlin shell element may generate polluting second-order transverse shear strain terms, which disturb the first-order distribution of the transverse shear strains $(\gamma_{xz},\ \gamma_{yz})$ afforded by the element and lead to shear locking. The polluting strain terms generated by $(\theta_x,\ \theta_y)$ can be filtered out by enriching the transverse displacement field (w) with a hierarchic transverse displacement field (w_h), which is a linear combination of higher-order hierarchic transverse displacement modes that are defined as polynomial functions of natural coordinates (ξ, η). The hierarchic transverse displacement modes $\boldsymbol{\Phi}_h^s$ can be used up to any order, where complete cubic and quartic displacement modes are considered for instance below:

$$w_h(\xi,\ \eta) = \boldsymbol{\Phi}_h^s\, \boldsymbol{\alpha}_h^s, \quad \boldsymbol{\Phi}_h^s = \langle\, \boldsymbol{\Phi}_h^3 \quad \boldsymbol{\Phi}_h^4 \quad \cdots \,\rangle \tag{17}$$

$$\boldsymbol{\Phi}_h^3 = \langle\, \Phi_{h,1}^3 \quad \Phi_{h,2}^3 \quad \Phi_{h,3}^3 \quad \Phi_{h,4}^3 \,\rangle \tag{18}$$

$$\boldsymbol{\Phi}_h^4 = \langle\, \xi\Phi_{h,1}^3 \quad \xi\Phi_{h,2}^3 \quad \xi\Phi_{h,3}^3 + \eta\Phi_{h,2}^3 \quad \eta\Phi_{h,3}^3 \quad \eta\Phi_{h,4}^3 \,\rangle \tag{19}$$

$$\Phi_{h,1}^3 = \xi^3 - \frac{3}{2}\xi^2 + \frac{1}{2}\xi, \quad \Phi_{h,2}^3 = \xi^2\eta - \frac{1}{2}\xi\eta \tag{20a}$$

$$\Phi_{h,3}^3 = \xi\eta^2 - \frac{1}{2}\xi\eta, \quad \Phi_{h,4}^3 = \eta^3 - \frac{3}{2}\eta^2 + \frac{1}{2}\eta \tag{20b}$$

where $\boldsymbol{\Phi}_h^3$ and $\boldsymbol{\Phi}_h^4$ are cubic and quartic hierarchic displacement modes for the 6-noded shell element, respectively, and $\boldsymbol{\alpha}_h^s$ are the associated hierarchic transverse shear strain parameters.

Accordingly, the hierarchic shear strains are expressed as:

$$\boldsymbol{\varepsilon}_h^s = \begin{Bmatrix} \gamma_{xzh} \\ \gamma_{yzh} \end{Bmatrix} = \begin{Bmatrix} \dfrac{\partial}{\partial x} \\ \dfrac{\partial}{\partial y} \end{Bmatrix} w_h = \boldsymbol{\Psi}_h^s\, \boldsymbol{\alpha}_h^s, \quad \boldsymbol{\Psi}_h^s = \begin{Bmatrix} \dfrac{\partial}{\partial x} \\ \dfrac{\partial}{\partial y} \end{Bmatrix} \boldsymbol{\Phi}_h^s \tag{21}$$

where $\boldsymbol{\Psi}_h^s$ denotes the hierarchic shear strain modes.

For curved shell elements, membrane locking may also occur if the

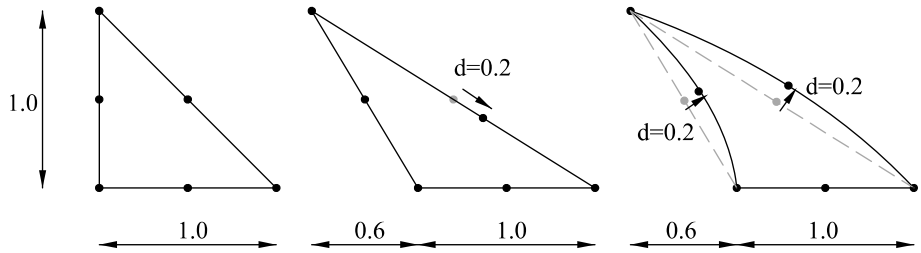

Fig. 5. Various element shapes for zero energy mode test of 6-noded shell element.

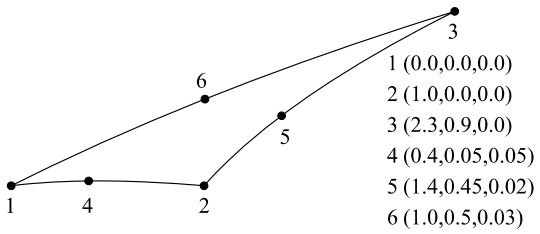

Fig. 6. Geometry of arbitrary 6-noded triangular element for isotropic element tests.

Table 2
Displacement modes considered in isotropic element test.

Mode	Displacement field	Mode	Displacement field	Mode	Displacement field
1	$u = ax$	9	$v = ax^2$	17	$\theta_y = axy$
2	$v = ay$	10	$\theta_x = ax$	18	$\theta_x = ay^2$
3	$u = ay$ or $v = ax$	11	$\theta_y = ay$	19	$\theta_y = ax^2$
4	$u = ax^2$	12	$\theta_x = ay$	20	$w = ax$
5	$v = ay^2$	13	$\theta_y = ax$	21	$w = ay$
6	$u = axy$	14	$\theta_x = ax^2$	22	$w = ax^2$
7	$v = axy$	15	$\theta_y = ay^2$	23	$w = ay^2$
8	$u = ay^2$	16	$\theta_x = axy$	24	$w = axy$

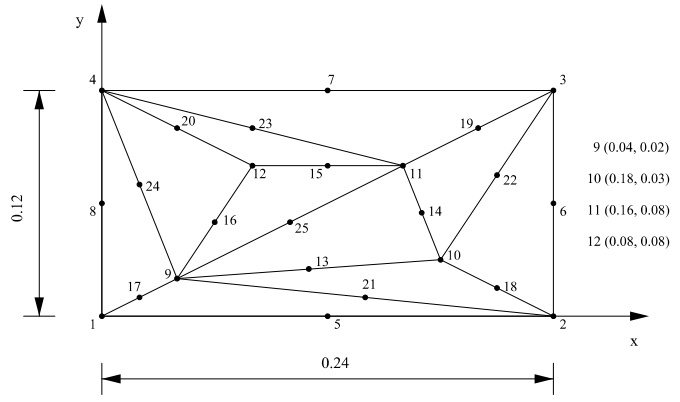

Fig. 7. Patch test for 6-noded shell elements (regular mesh).

element undergoes transverse displacement (w), where the local geometric nonlinear strain terms associated with the transverse displacement, as indicated in Eq. (11a), are of higher-order spatial distribution than the strain terms that are afforded by planar displacements (u, v). Consequently, the curved shell element cannot deform in any arbitrary transverse mode (w), as allowed by its transverse DOFs, without polluting $(\varepsilon_x,\ \varepsilon_y,\ \gamma_{xy})$ with higher-order terms, resulting in an overestimation of the membrane strain energy. The polluting strain terms induced by (w) can be offset by enriching the planar displacement fields (u, v) with hierarchic planar displacement fields $(u_h,\ v_h)$, which contain

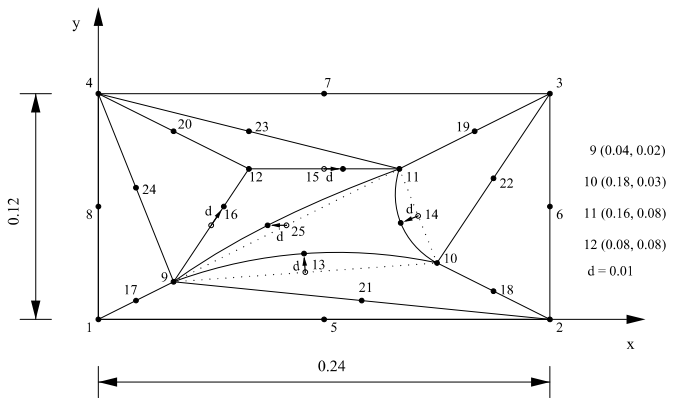

Fig. 8. Patch test for 6-noded shell elements (distorted mesh).

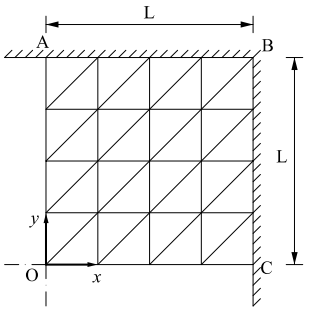

Fig. 9. A 4 × 4 quarter-model of clamped square plate subjected to uniform load.

higher-order hierarchic planar modes beyond those used in (u, v). Again, the optimisation approach can utilise hierarchic modes up to any order, where complete cubic and quartic modes are provided for instance in the following:

$$\begin{Bmatrix} u_h(\xi,\eta) \\ v_h(\xi,\eta) \end{Bmatrix} = \boldsymbol{\Phi}_h^m\, \boldsymbol{\alpha}_h^m, \quad \boldsymbol{\Phi}_h^m = \begin{bmatrix} \boldsymbol{\Phi}_h^3 & \mathbf{0} & \boldsymbol{\Phi}_h^4 & \mathbf{0} & \cdots \\ \mathbf{0} & \boldsymbol{\Phi}_h^3 & \mathbf{0} & \boldsymbol{\Phi}_h^4 & \cdots \end{bmatrix} \tag{22}$$

in which $\boldsymbol{\Phi}_h^m$ contains hierarchic membrane strain-inducing displacement modes in terms of natural coordinates (ξ,η), and $\boldsymbol{\alpha}_h^m$ are the associated hierarchic planar strain parameters; $\boldsymbol{\Phi}_h^3$ and $\boldsymbol{\Phi}_h^4$ are respectively the cubic and quartic hierarchic displacement modes given previously in Eqs 18–20.

The resulting hierarchic membrane strains can then be derived from:

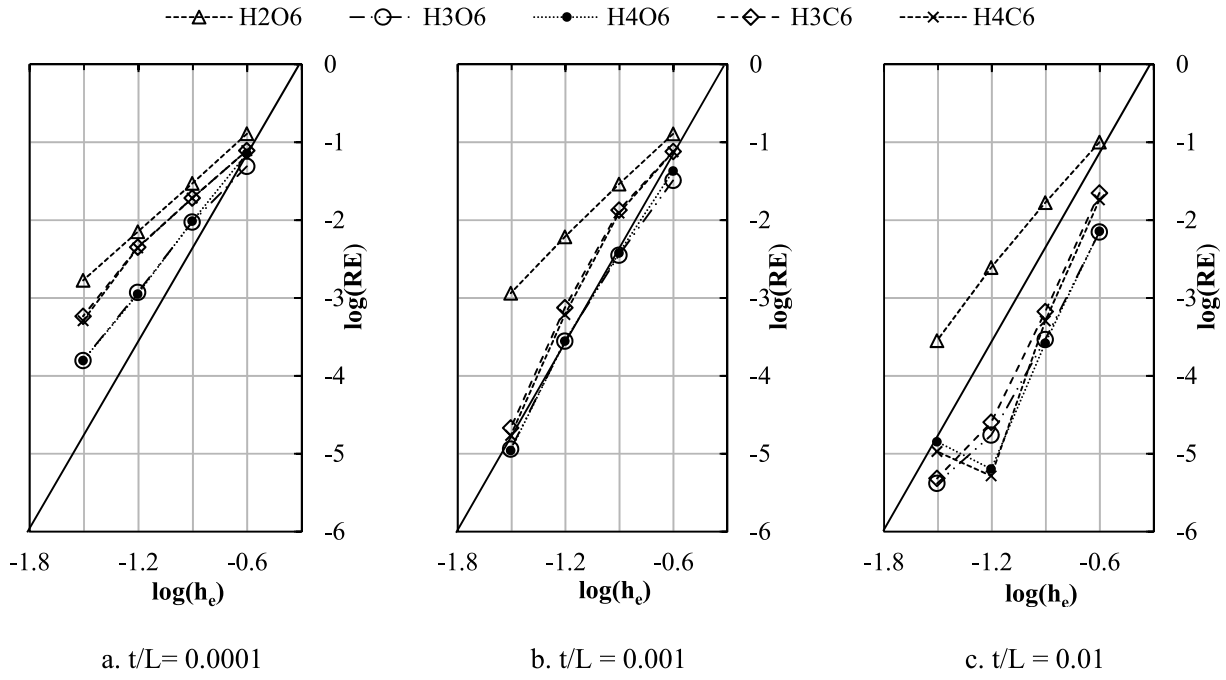

Fig. 10. Convergence curves of variants of optimised 6-noded elements for clamped square plate problem.

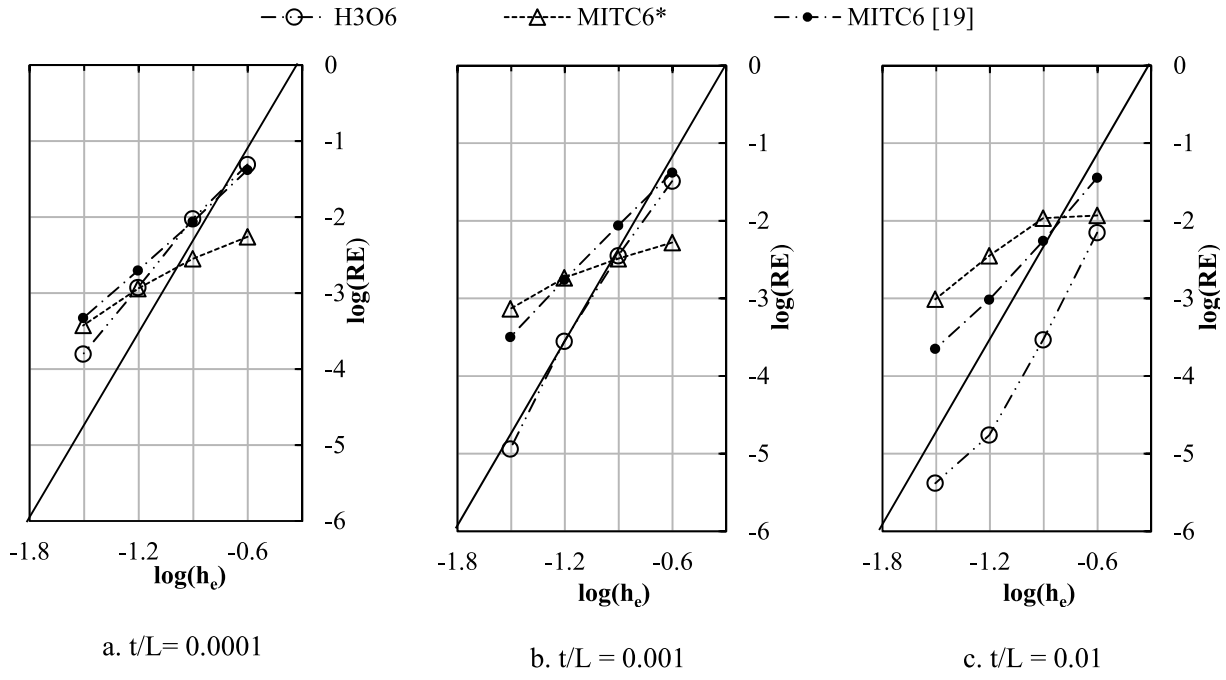

Fig. 11. Convergence curves of H3O6 and MITC6* in comparison with MITC6 for clamped square plate problem.

$$\boldsymbol{\varepsilon}_h^m = \begin{Bmatrix} \varepsilon_{xh} \\ \varepsilon_{yh} \\ \gamma_{xyh} \end{Bmatrix} = \begin{bmatrix} \frac{\partial}{\partial x} & 0 \\ 0 & \frac{\partial}{\partial y} \\ \frac{\partial}{\partial y} & \frac{\partial}{\partial x} \end{bmatrix} \begin{Bmatrix} u_h \\ v_h \end{Bmatrix} = \boldsymbol{\Psi}_h^m \boldsymbol{\alpha}_h^m, \quad \boldsymbol{\Psi}_h^m = \begin{bmatrix} \frac{\partial}{\partial x} & 0 \\ 0 & \frac{\partial}{\partial y} \\ \frac{\partial}{\partial y} & \frac{\partial}{\partial x} \end{bmatrix} \boldsymbol{\Phi}_h^m \tag{23}$$

where $\boldsymbol{\Psi}_h^m$ represents the hierarchic membrane strain modes.

As noted in Section 3.2, the objective strain modes are initially defined as complete polynomial functions in terms of physical (x, y) coordinates, which readily addresses locking due to polluting higher-order terms as a result of distortion in the isoparametric element shape. For a complete treatment of distortion locking in a shell element, it is also necessary to filter out the polluting bending strain terms due to element distortion. Although the bending strains exhibit no sign of locking for regular element shapes, as implied by Eq. (11b), this is, however, not the case for distorted elements, where the non-constant Jacobian matrix **J** results in conforming bending strains that are non-polynomial in terms of physical coordinates, thus leading to locking

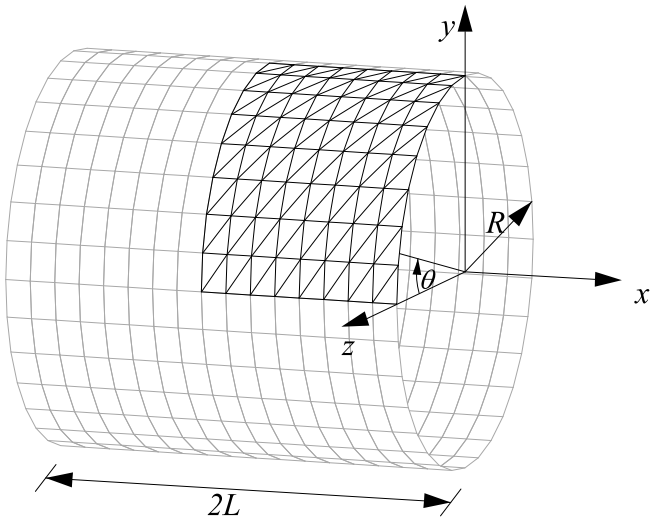

Fig. 12. An octant model of cylindrical shell with 6-noded shell elements.

due to polluting non-polynomial approximation. The transformation of the conforming to assumed bending strains can be shown to be identical to that relating the conforming and assumed membrane strains. The objective and hierarchic bending strain modes, $\boldsymbol{\Psi}_o^b$ and $\boldsymbol{\Psi}_h^b$, are respectively given by Eqs (15) and (24):

$$\boldsymbol{\Psi}_h^b = \boldsymbol{\Psi}_h^m \tag{24}$$

In order to ensure that the proposed elements pass the constant mode patch tests, all hierarchic correcting strain modes require zero mean values throughout the element domain [24]. Therefore, an additional measure is taken to enforce zero mean constraints on each hierarchic strain mode, which is achieved via integration over the physical element domain Ω^e as follows:

$$\overline{\boldsymbol{\Psi}}_h^m = \boldsymbol{\Psi}_h^m - \frac{\int_{\Omega^e} \boldsymbol{\Psi}_h^m \, d\Omega^e}{\Omega^e}, \quad \overline{\boldsymbol{\Psi}}_h^b = \overline{\boldsymbol{\Psi}}_h^m \tag{25a}$$

$$\overline{\boldsymbol{\Psi}}_h^s = \boldsymbol{\Psi}_h^s - \frac{\int_{\Omega^e} \boldsymbol{\Psi}_h^s \, d\Omega^e}{\Omega^e} \tag{25b}$$

Accordingly, the modified hierarchic correcting strain modes $\overline{\boldsymbol{\Psi}}_h^m$, $\overline{\boldsymbol{\Psi}}_h^b$, and $\overline{\boldsymbol{\Psi}}_h^s$ replace the original modes $\boldsymbol{\Psi}_h^m$, $\boldsymbol{\Psi}_h^b$, and $\boldsymbol{\Psi}_h^s$ in performing the hierarchic optimisation, as given by:

$$\left(\int_{\Omega^e} \begin{bmatrix} \overline{\boldsymbol{\Psi}}_h^{r\mathrm{T}} \overline{\boldsymbol{\Psi}}_h^r & -\overline{\boldsymbol{\Psi}}_h^{r\mathrm{T}} \boldsymbol{\Psi}_o^r \\ -\boldsymbol{\Psi}_o^{r\mathrm{T}} \overline{\boldsymbol{\Psi}}_h^r & \boldsymbol{\Psi}_o^{r\mathrm{T}} \boldsymbol{\Psi}_o^r \end{bmatrix} \mathrm{d}\Omega^e \right) \begin{Bmatrix} \boldsymbol{\alpha}_h^r \\ \boldsymbol{\alpha}_o^r \end{Bmatrix} = \int_{\Omega^e} \begin{bmatrix} -\overline{\boldsymbol{\Psi}}_h^{r\mathrm{T}} \\ \boldsymbol{\Psi}_o^{r\mathrm{T}} \end{bmatrix} \boldsymbol{\varepsilon}^r \, \mathrm{d}\Omega^e \quad (r = m, b, s) \tag{26}$$

where r denotes the membrane (m), bending (b) or transverse shear (s) strain modes; the objective strain modes $\boldsymbol{\Psi}_o^m$, $\boldsymbol{\Psi}_o^b$ and $\boldsymbol{\Psi}_o^s$ are given by Eqs (12), (15) and (16), respectively; and the hierarchic correcting strain modes $\overline{\boldsymbol{\Psi}}_h^m$, $\overline{\boldsymbol{\Psi}}_h^b$ and $\overline{\boldsymbol{\Psi}}_h^s$ are given by Eq (25a-b), respectively. For each of the three strain sets, the strain parameters $\boldsymbol{\alpha}_h^r$ and $\boldsymbol{\alpha}_o^r$ ($r = m, b, s$) can be obtained through numerical integration on Eq. (26), and an assumed strain distribution, in the form of Eq. (6) (replacing $\boldsymbol{\Psi}_{h\,(i)}$ with $\overline{\boldsymbol{\Psi}}_{h\,(i)}$) or Eq. (7), can then be derived depending on the variant element under consideration.

3.4. Spatial isotropy of optimised triangular elements

The aforementioned hierarchic optimisation approach improves the strain distribution via the minimisation of a functional integrating the square of the strain error $(\boldsymbol{\varepsilon} + \boldsymbol{\varepsilon}_h - \boldsymbol{\varepsilon}_o)$ over the element domain, which is not spatially isotropic, as can be inferred from examining the strain tensor. The optimisation of transverse shear strains turns out to be isotropic, owing to the fact that these strain components transform spatially according to a first-order tensor transformation. However, this is not the case for the optimisation of either the membrane strains or the curvature strains, resulting from a second-order tensor transformation of these strains. Since the associated objective functional is not spatially invariant, in the sense that it varies when the same component strains are transformed to a different system, the resulting element stiffness is not invariant to the choice of the local coordinate system, which is un-

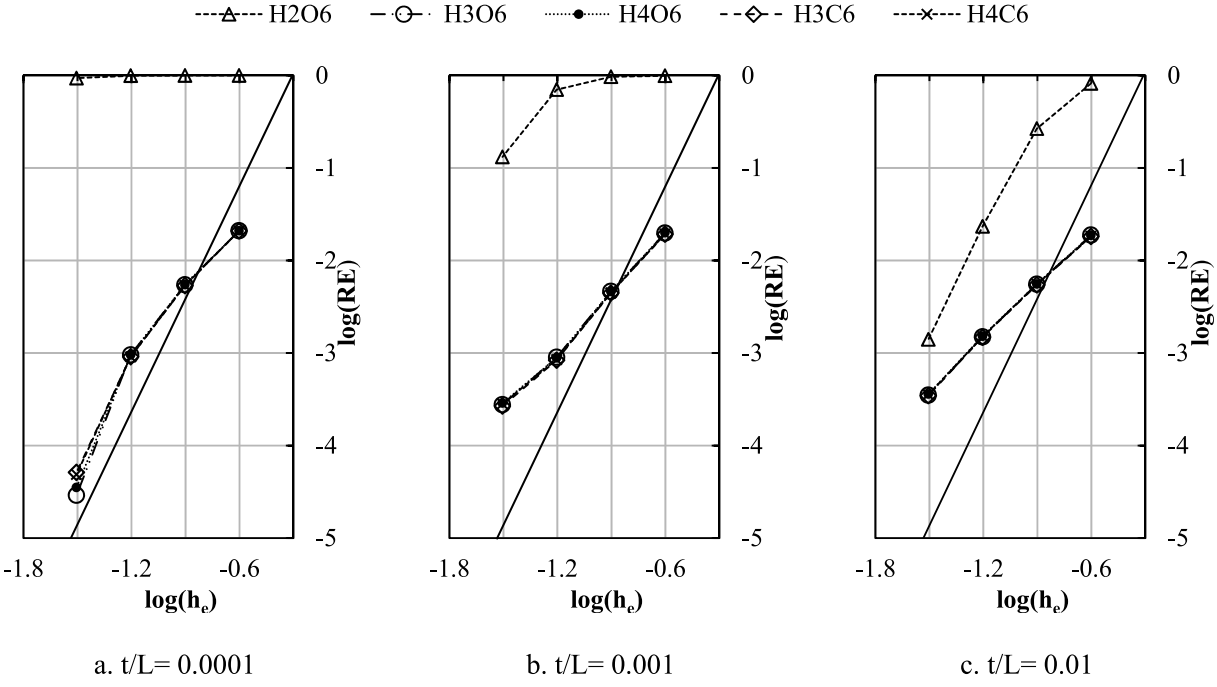

Fig. 13. Convergence curves of variants of optimised 6-noded elements for cylindrical shell with both ends free.

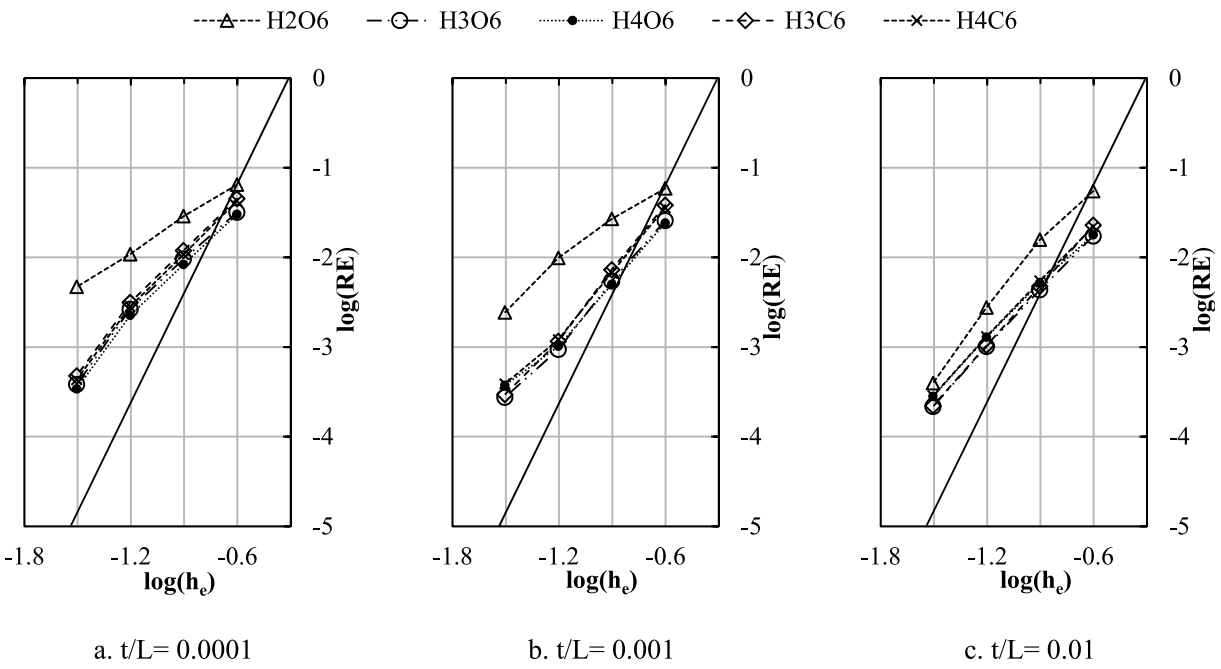

Fig. 14. Convergence curves of variants of optimised 6-noded elements for cylindrical shell with both ends clamped.

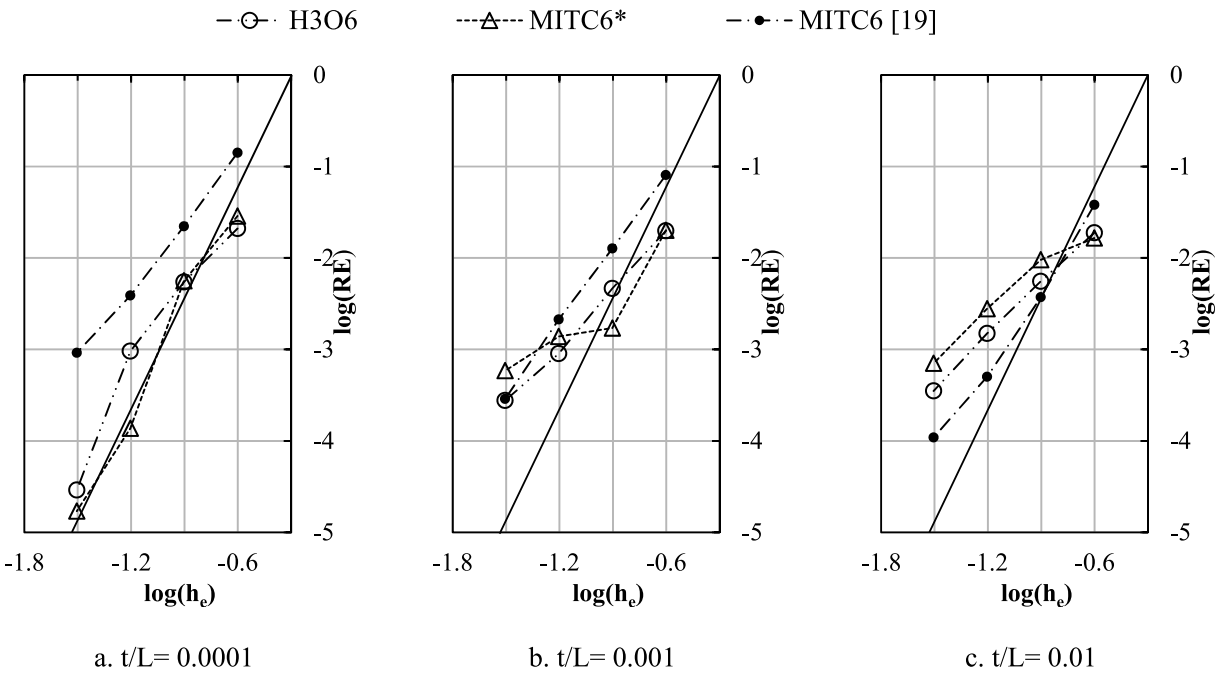

Fig. 15. Convergence curves of H3O6 and MITC6* in comparison with MITC6 for cylindrical shell with both ends free.

desirable in practical applications [18,23,25].

In order to achieve nodal invariance for the optimised 6-noded triangular elements, the optimisation of membrane and curvature strains can be modified. Herein, rather than enhancing the membrane strain components $(\varepsilon_x, \varepsilon_y, \gamma_{xy})$, the three membrane strains along the element edges $(\varepsilon_{12}, \varepsilon_{23}, \varepsilon_{31})$ are optimised, as illustrated in Fig. 2. The objective functional expressed in terms of these strains becomes invariant to nodal ordering, leading to the outcome of the optimisation process achieving the nodal invariance characteristic. Accordingly, the following steps are taken to for the hierarchic optimisation on membrane strains for the 6-noded shell element:

(i) Transform membrane strains $\boldsymbol{\varepsilon}^m$ to edge-based strains $(\varepsilon_{12}, \varepsilon_{23}, \varepsilon_{31})$:

$$\boldsymbol{\varepsilon}_\Delta = \begin{Bmatrix} \varepsilon_{12} \\ \varepsilon_{23} \\ \varepsilon_{31} \end{Bmatrix} = \mathbf{T}_\Delta \boldsymbol{\varepsilon}^m, \quad \mathbf{T}_\Delta = \begin{bmatrix} \widehat{c}_1^2 & \widehat{s}_1^2 & \widehat{c}_1\widehat{s}_1 \\ \widehat{c}_2^2 & \widehat{s}_2^2 & \widehat{c}_2\widehat{s}_2 \\ \widehat{c}_3^2 & \widehat{s}_3^2 & \widehat{c}_3\widehat{s}_3 \end{bmatrix} \tag{27}$$

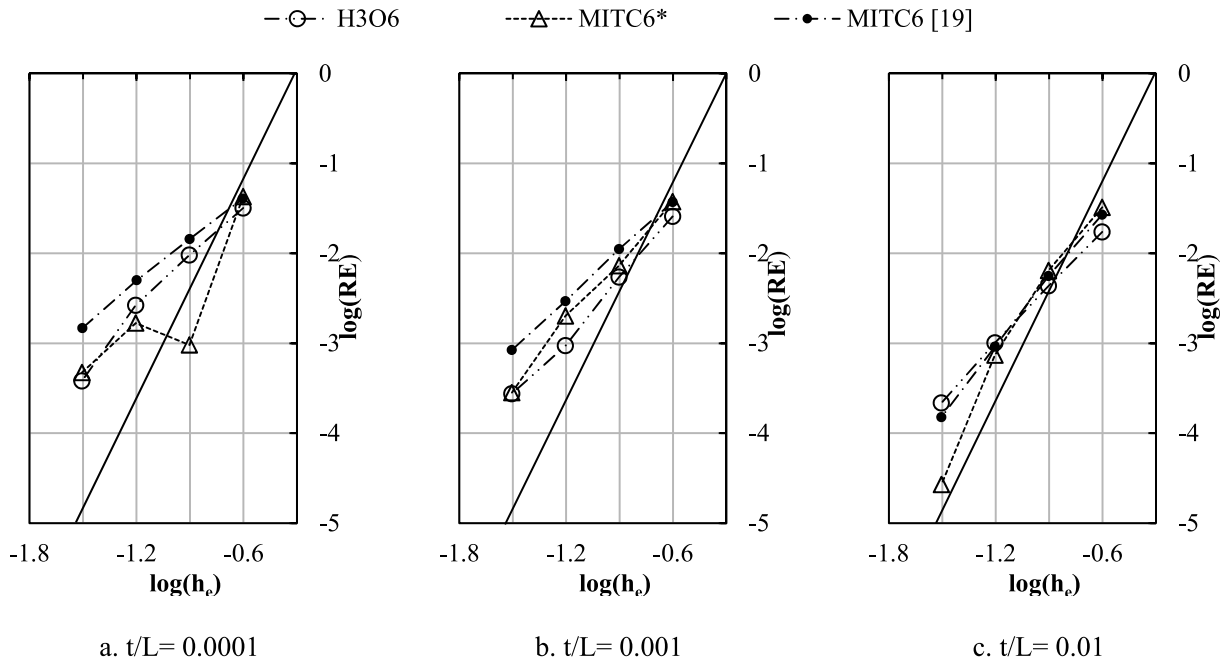

Fig. 16. Convergence curves of H3O6 and MITC6* in comparison with MITC6 for the cylindrical shell problem where both ends are clamped.

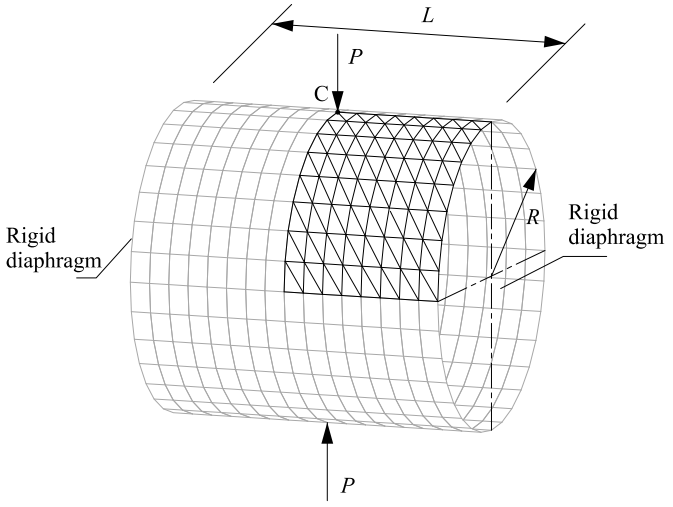

Fig. 17. An octant model of pinched cylindrical shell supported by rigid diaphragms.

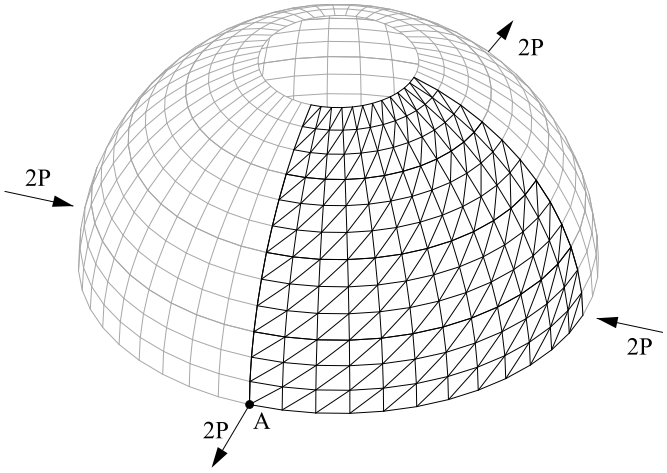

Fig. 18. A quarter model of the pinched hemispherical shell with an 18° cut-off.

Table 3
Normalised deflections at the point of loading for the pinched cylinder problem.

Acronym key	4 × 4	8 × 8	12 × 12
CNF6	0.14	0.49	0.74
H2O6	0.39	0.71	0.88
H3O6	0.73	0.92	0.98
H4O6	0.76	0.92	0.98
H3C6	0.60	0.89	0.96
H4C6	0.65	0.91	0.97
MITC6*	0.44	0.83	0.96
M6-3 (Bucalem et al. [20])	0.64	0.90	0.98
M7-3 (Bucalem et al. [20])	1.19	1.13	1.10

where $\varepsilon_{i\,i_+}$ ($i = 1, 2, 3$) is the direct strain in the direction of edge i-i_+; $\widehat{c}_i$ and $\widehat{s}_i$ are respectively the cosine and sine values of the angle from the local x-axis to the edge i-i_+.

Table 4
Normalised deflections at point A for the pinched hemispherical shell problem (triangular element meshes).

Acronym key	Regular mesh			Distorted mesh		
	4 × 4	8 × 8	16 × 16	4 × 4	8 × 8	16 × 16
CNF6	0.01	0.13	0.42	0.01	0.07	0.26
H2O6	0.05	0.34	0.70	0.05	0.19	0.49
H3O6	0.88	0.99	0.99	0.45	0.95	0.99
H4O6	0.91	0.99	0.99	0.59	0.97	0.99
H3C6	0.69	0.98	0.99	0.21	0.91	0.99
H4C6	0.78	0.98	0.99	0.37	0.94	0.99
MITC6*	0.63	0.95	0.99	0.23	0.84	0.96
M6-3 (Bucalem et al. [20])	0.16	0.66	0.87	–	–	–
M7-3 (Bucalem et al. [20])	0.65	0.91	0.96	–	–	–

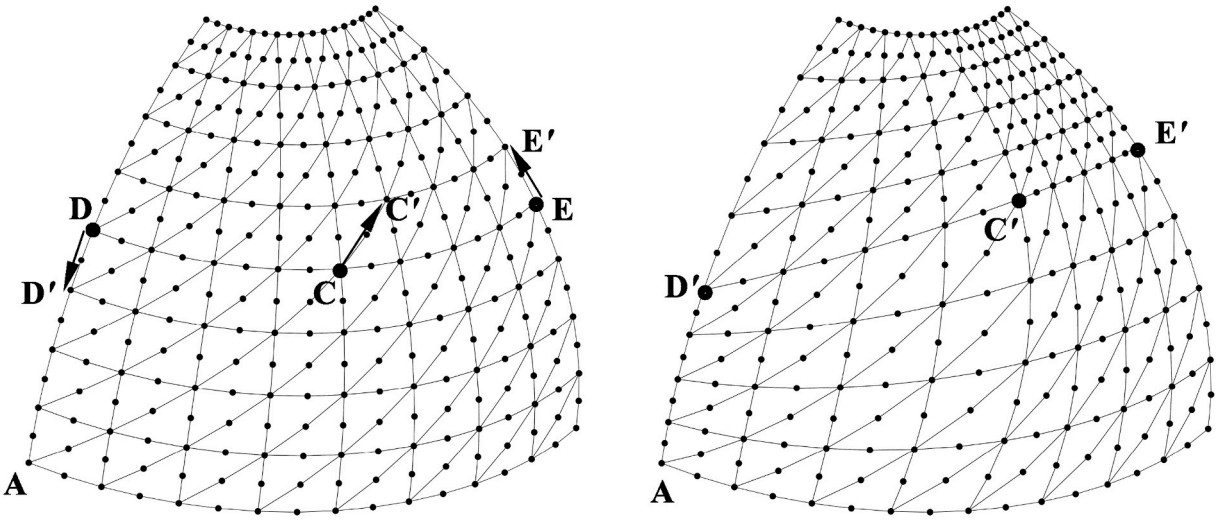

Fig. 19. Pinched hemispherical shell with an 18° cut-off (distorted mesh).

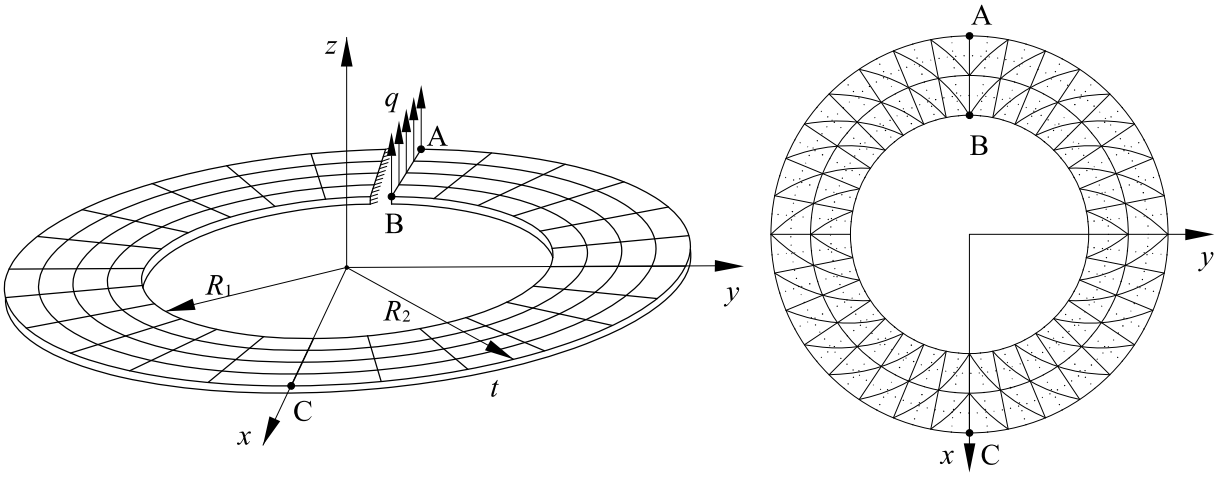

Fig. 20. Annular plate subject to uniform transverse loading.

(ii) The hierarchic and objective strain modes for edge strains, denoted as $\overline{\boldsymbol{\Psi}}_h^{\Delta}$ and $\boldsymbol{\Psi}_o^{\Delta}$, respectively, are obtained from the following transformation:

$$\overline{\boldsymbol{\Psi}}_h^{\Delta} = \mathbf{T}_{\Delta}\overline{\boldsymbol{\Psi}}_h^{m}, \quad \boldsymbol{\Psi}_o^{\Delta} = \mathbf{T}_{\Delta}\boldsymbol{\Psi}_o^{m} \tag{28}$$

(iii) Replacing Eq. (26), the following equation is used for hierarchic optimisation on the three edge-based strains $(\varepsilon_{12}, \varepsilon_{23}, \varepsilon_{31})$:

$$\left(\int_{\Omega^e}\left[\begin{array}{c|c}\overline{\boldsymbol{\Psi}}_h^{\Delta T}\overline{\boldsymbol{\Psi}}_h^{\Delta} & -\overline{\boldsymbol{\Psi}}_h^{\Delta T}\boldsymbol{\Psi}_o^{\Delta} \\ \hline -\boldsymbol{\Psi}_o^{\Delta T}\overline{\boldsymbol{\Psi}}_h^{\Delta} & \boldsymbol{\Psi}_o^{\Delta T}\boldsymbol{\Psi}_o^{\Delta}\end{array}\right] d\Omega^e\right)\left\{\begin{array}{c}\boldsymbol{\alpha}_h^m \\ \hline \boldsymbol{\alpha}_o^m\end{array}\right\} = \int_{\Omega^e}\left[\begin{array}{c}-\overline{\boldsymbol{\Psi}}_h^{\Delta T}\mathbf{T}_{\Delta} \\ \hline \boldsymbol{\Psi}_o^{\Delta T}\mathbf{T}_{\Delta}\end{array}\right]\boldsymbol{\varepsilon}^m\, d\Omega^e \tag{29}$$

(iv) Thus, as before, parameters $\boldsymbol{\alpha}_h^m$ and $\boldsymbol{\alpha}_o^m$ are numerically solved for using Gaussian quadrature in terms of the conforming strains component in the local *x*-*y* system:

$$\boldsymbol{\alpha}_h^m = \boldsymbol{\Gamma}_h\left\{\begin{array}{c}\boldsymbol{\varepsilon}_{(1)}^m \\ \vdots \\ \boldsymbol{\varepsilon}_{(i)}^m \\ \vdots\end{array}\right\}, \quad \boldsymbol{\alpha}_o^m = \boldsymbol{\Gamma}_o\left\{\begin{array}{c}\boldsymbol{\varepsilon}_{(1)}^m \\ \vdots \\ \boldsymbol{\varepsilon}_{(i)}^m \\ \vdots\end{array}\right\} \tag{30}$$

with the subscript (*i*) representing the *i*th Gauss point.

(v) The enhanced membrane strains $(\varepsilon_x, \varepsilon_y, \gamma_{xy})$ at the Gauss points are then derived in either the corrective or the objective strain form:

$$\left\{\begin{array}{c}\widetilde{\boldsymbol{\varepsilon}}_{(1)}^m \\ \vdots \\ \widetilde{\boldsymbol{\varepsilon}}_{(i)}^m \\ \vdots\end{array}\right\} = \widetilde{\mathbf{T}}_m\left\{\begin{array}{c}\boldsymbol{\varepsilon}_{(1)}^m \\ \vdots \\ \boldsymbol{\varepsilon}_{(i)}^m \\ \vdots\end{array}\right\}, \quad \widetilde{\mathbf{T}}_m = \mathbf{I} + \left[\begin{array}{c}\overline{\boldsymbol{\Psi}}_{h(1)}^m \\ \vdots \\ \overline{\boldsymbol{\Psi}}_{h(i)}^m \\ \vdots\end{array}\right]\boldsymbol{\Gamma}_h \quad \text{(Corrective)} \tag{31}$$

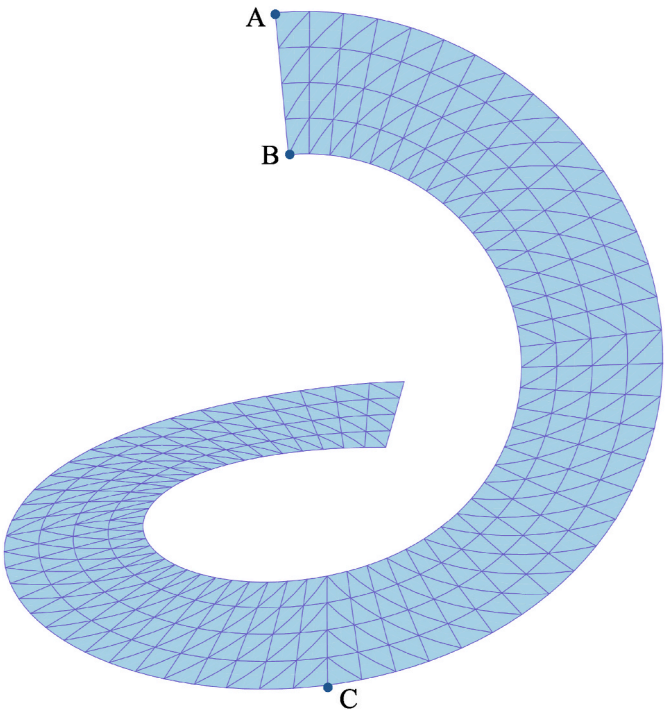

Fig. 21. Deformed configuration of annular plate.

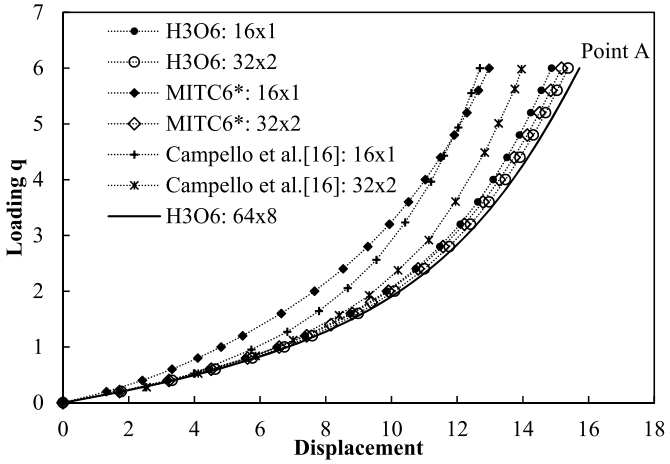

Fig. 22. Equilibrium paths of vertical displacement at Point A for annular plate.

$$\begin{Bmatrix} \widehat{\boldsymbol{\varepsilon}}^m_{(1)} \\ \vdots \\ \widehat{\boldsymbol{\varepsilon}}^m_{(i)} \\ \vdots \end{Bmatrix} = \widehat{\mathbf{T}}_m \begin{Bmatrix} \boldsymbol{\varepsilon}^m_{(1)} \\ \vdots \\ \boldsymbol{\varepsilon}^m_{(i)} \\ \vdots \end{Bmatrix}, \quad \widehat{\mathbf{T}}_m = \begin{bmatrix} \boldsymbol{\Psi}^m_{o(1)} \\ \vdots \\ \boldsymbol{\Psi}^m_{o(i)} \\ \vdots \end{bmatrix} \boldsymbol{\Gamma}_o \quad \text{(Objective)} \qquad (32)$$

The hierarchic optimisation for the curvature strains follows the same steps. By modifying the optimisation procedure for membrane and curvature strains, whilst retaining the previous procedure in Section 3.3 for optimising transverse shear strains, a spatially isotropic local formulation of a lock-free triangular element is achieved.

As previously noted, the corrective (C) and objective (O) alternative approaches lead to two variants of the 6-noded triangular shell element, denoted respectively by H*m*C6 and H*m*O6, in which optimisation with

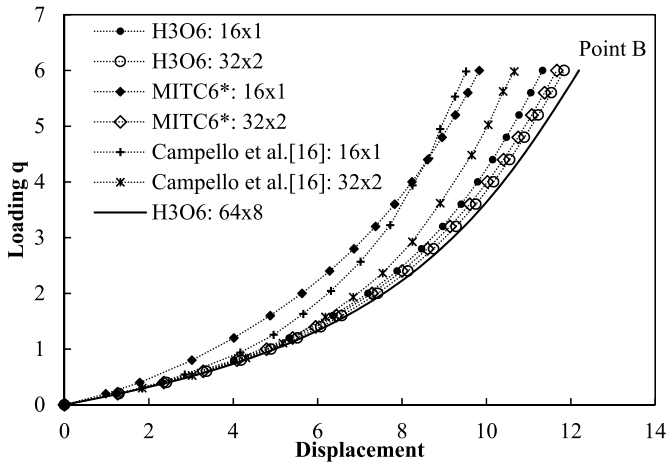

Fig. 23. Equilibrium paths of vertical displacement at Point B for annular plate.

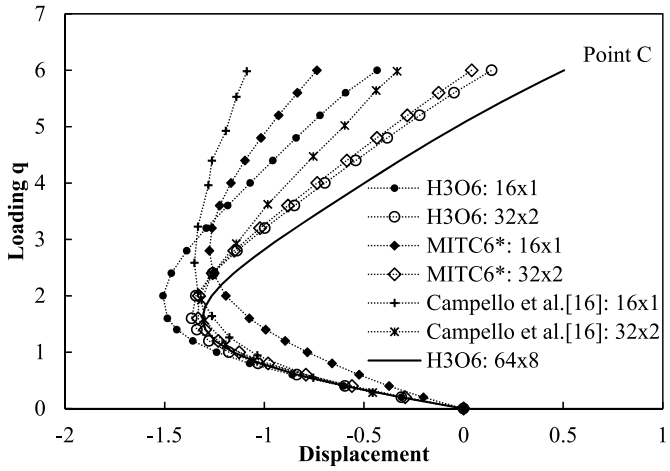

Fig. 24. Equilibrium paths of vertical displacement at Point C for annular plate.

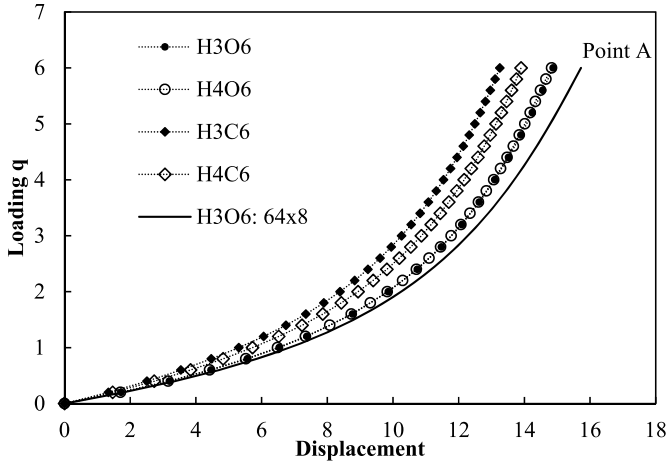

Fig. 25. Equilibrium paths of vertical displacement at Point A with various optimised 6-noded elements for 16 × 1 mesh.

hierarchic (H) modes up to any complete polynomial order ($m = 3, 4, \ldots$) can be applied. For instance, H3O6 represents an objective strain element with 3rd order hierarchic correction modes, while H4C6 represents a corrective strain element with 4th order hierarchic correction modes. It is even possible for the optimisation to be undertaken without

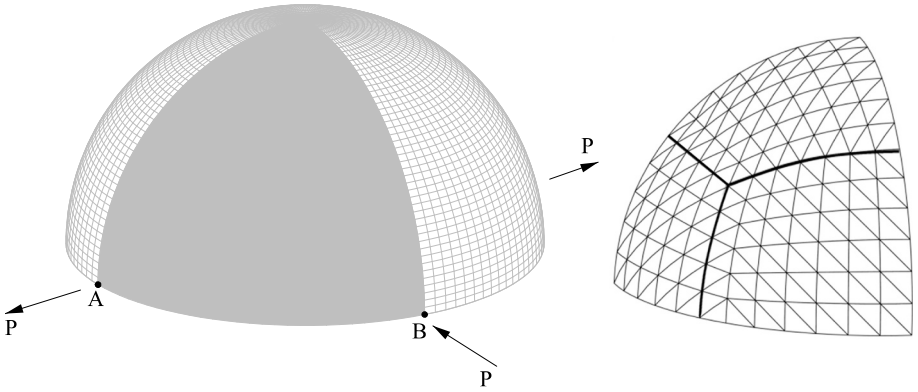

Fig. 26. Hemispherical shell subject to symmetric concentrated forces at base and 6 × 6 mesh pattern.

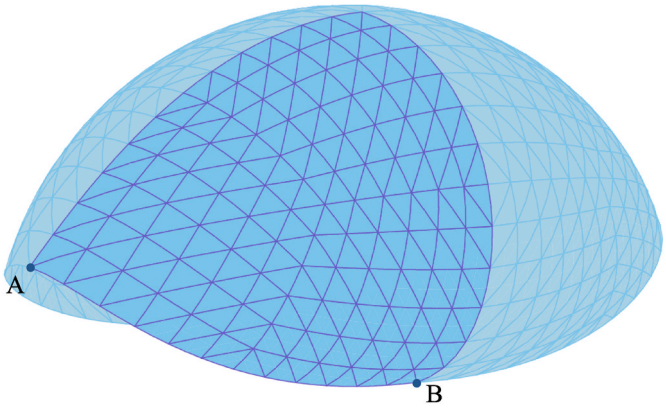

Fig. 27. Deformed configuration of hemispherical shell.

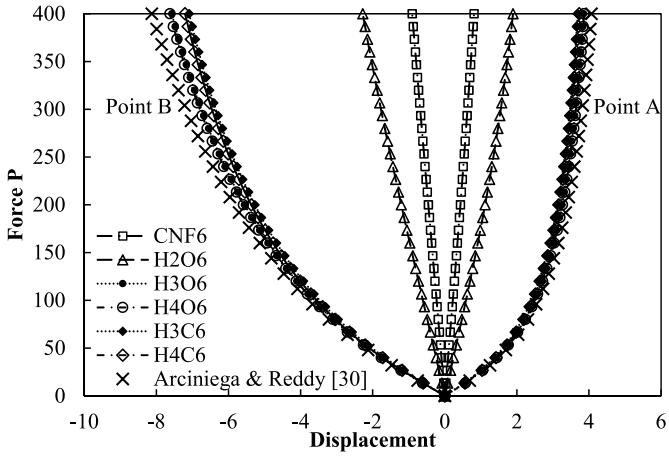

a. 3×3 mesh

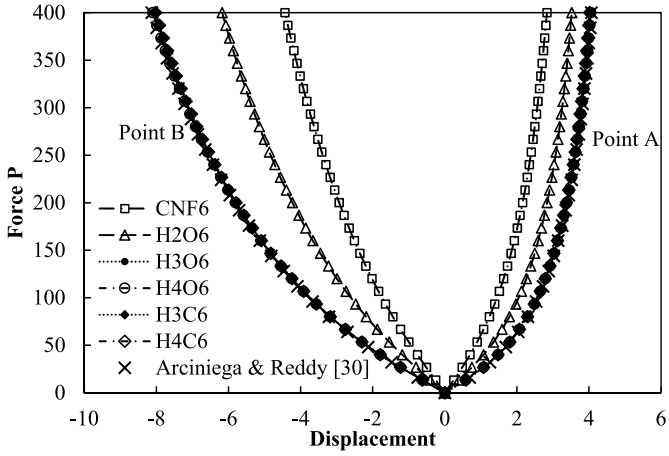

b. 6×6 mesh

Fig. 28. Load-displacement curves of radial displacements with different meshes of various optimised 6-noded elements.

hierarchic correction modes, in which case the assumed strains are the objective strains that offer a best fit of the conforming strains, leading to an element denoted by H2O6.

4. Zero-macrospin co-rotational coordinate system

In order to enable large-displacement geometrically nonlinear analysis, the local triangular element formulations established in the previous section are framed in a co-rotational coordinate system employing the 'zero-macrospin' definition [23], which excludes rigid-body rotations from the local kinematics at the macro element level and fulfils the important characteristics of simplicity and nodal invariance. The co-rotational system used for the 6-noded triangular element is briefly presented in the following.

Fig. 3 shows a unit square area, defined by orthogonal unit vectors $\mathbf{c}_x$ and $\mathbf{c}_y$, which is subjected to a uniform planar 'stretch' operation in any two orthogonal directions leading to transformed vectors $\mathbf{c}'_x$ and $\mathbf{c}'_y$. It can be shown that $\mathbf{c}_x$ is always obtained as the normalised sum of $\mathbf{c}'_x$ and $\mathbf{c}'^n_y$, where $\mathbf{c}'^n_y$ is a planar rotation of $\mathbf{c}'_y$ by $-\pi/2$, and $\mathbf{c}_y$ is similarly obtained as the normalised sum of $\mathbf{c}'_y$ and $\mathbf{c}'^n_x$, where $\mathbf{c}'^n_x$ is a planar rotation of $\mathbf{c}'_x$ by $\pi/2$. Accordingly, if $\mathbf{c}_z$ is known, the remaining vectors of the triad are obtained from the stretched vectors as [23]:

$$\mathbf{c}_x = \frac{\mathbf{c}'_x + \mathbf{c}'^n_y}{\left|\mathbf{c}'_x + \mathbf{c}'^n_y\right|}, \quad \mathbf{c}'^n_y = \mathbf{c}'_y \times \mathbf{c}_z, \quad \mathbf{c}_y = \mathbf{c}_z \times \mathbf{c}_x \tag{33}$$

With reference to Fig. 4, in the initial undeformed configuration of a 6-noded curved shell element, the unit vector $\mathbf{c}^o_z$ is defined to be normal to the element plane formed by the three corner nodes. The orthogonal unit vectors $\mathbf{c}^o_x$ and $\mathbf{c}^o_y$ are defined such that $\mathbf{c}^o_x$ is aligned with edge 1–2.

In the deformed configuration, the unit vector $\mathbf{c}_z$ is still taken as normal to the deformed element plane formed by the corner nodes:

$$\mathbf{c}_z = \frac{\mathbf{v}_{12} \times \mathbf{v}_{23}}{|\mathbf{v}_{12} \times \mathbf{v}_{23}|} \tag{34}$$

where $\mathbf{v}_{ij}$ is the vector connecting node i to node j in the current

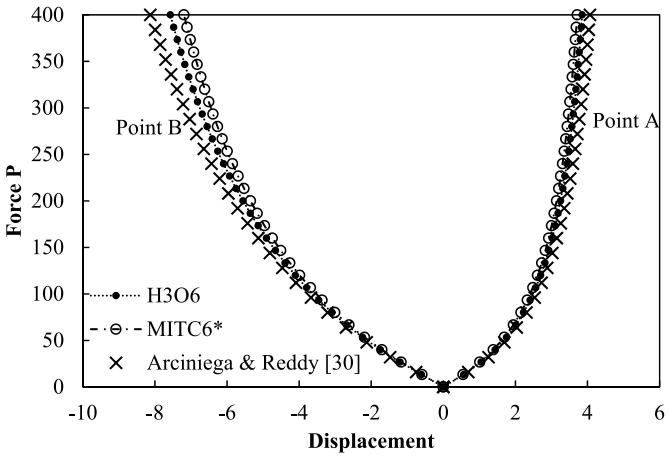

a. 3×3 mesh

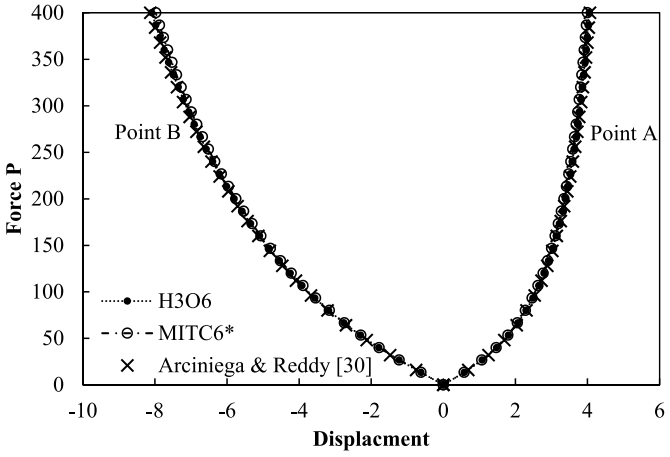

b. 6×6 mesh

Fig. 29. Load-displacement curves of radial displacements with different meshes of H3O6 and MITC6* elements.

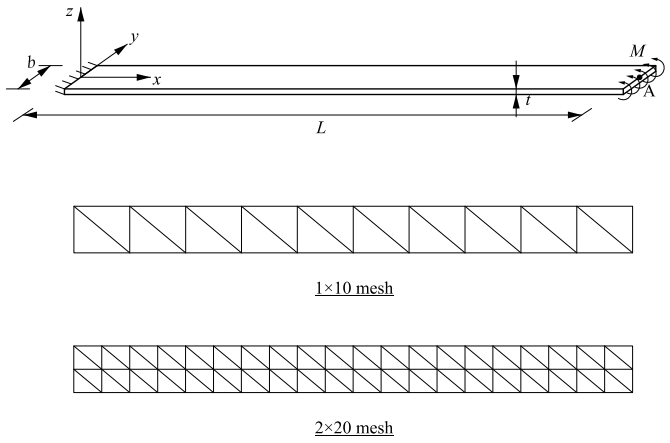

Fig. 30. Cantilever beam loaded with end moment.

configuration.

The stretched vectors $\mathbf{c}_x'$ and $\mathbf{c}_y'$ for the triangular element are linked to the nodal coordinates in the current deformed configuration using an expression of the form [23]:

$$\mathbf{c}_x' = a_{x1}\mathbf{v}_{12} + a_{x2}\mathbf{v}_{23}, \quad \mathbf{c}_y' = a_{y1}\mathbf{v}_{12} + a_{y2}\mathbf{v}_{23} \tag{35}$$

in which the scaling parameters are determined with reference to the initial geometric configuration of the element as:

$$a_{x1} = \frac{1}{|\mathbf{v}_{12}^o|}, \quad a_{x2} = 0,$$
$$a_{y1} = -\frac{\mathbf{c}_{12}^{o\,T}\mathbf{c}_{23}^o}{|\mathbf{v}_{12}^o|\sqrt{1-(\mathbf{c}_{12}^{o\,T}\mathbf{c}_{23}^o)^2}}, \quad a_{y2} = \frac{1}{|\mathbf{v}_{23}^o|\sqrt{1-(\mathbf{c}_{12}^{o\,T}\mathbf{c}_{23}^o)^2}} \tag{36}$$

$$\mathbf{c}_{ij}^o = \frac{\mathbf{v}_{ij}^o}{|\mathbf{v}_{ij}^o|} \tag{37}$$

where $\mathbf{v}_{ij}^o$ is the vector connecting node i to node j in the initial configuration.

With the stretched vectors $\mathbf{c}_x'$ and $\mathbf{c}_y'$ obtained according to Eq. (35), the rotated unit vectors $\mathbf{c}_x$ and $\mathbf{c}_y$, defining the current orientation of the local co-rotational system, can now be established from the inverse 'stretch' operation given by Eq. (33). Details of the transformations between the global and local systems are provided in Ref. [23], including i) the transformation of global to local nodal displacements, ii) the transformation of local to global forces, and iii) the transformation of the local to global tangent stiffness matrix.

It is worth noting that in terms of global DOFs, two approaches are applicable:

- For smooth plate and curved shell surfaces without branched intersection, each node utilises 5 global DOFs, including 3 translational DOFs and 2 rotational DOFs. At each node, two rotations are sufficient to relate the orientation of the nodal normal in the current configuration to its orientation in the initial configuration. Therefore, for smooth plates and curved shells with no branched intersection, at each node, the two components of the nodal normal which are smallest in absolute value may be chosen as the two global nodal rotational DOFs [23,26].
- For non-smooth shell surfaces or plate and shell surfaces with branched intersection, the nodes along the non-smooth edge or branched intersection are associated with 6 global DOFs, including 3 translational DOFs and 3 rotational DOFs.

In both approaches, the global nodal rotational DOFs determine the orientation of the normal at each of the element nodes, which, along with the global nodal translational DOFs, determine the local element DOFs described in Section 3.1 according to the current orientation of the local co-rotational reference system [23].

Finally, it is worth noting that even though the adopted zero macro-spin co-rotational system can be applied to large-strain problems, the focus of this paper is on its application to small-strain large-displacement problems.

5. Numerical examples

The optimised 6-noded shell elements proposed in this paper have been implemented in ADAPTIC [27] v2.14.4, which is used hereafter in several numerical examples to investigate and demonstrate the efficiency and accuracy of the new shell element variants. For comparison purposes, a 6-noded Reissner-Mindlin shell element employing the MITC6 strain-mapping scheme [19] for the local element response is also considered within the same co-rotational approach for large displacement analysis, which is represented by the acronym key 'MITC6*'. The asterisk symbol '*' indicates that there are minor differences of the element from the original MITC6 element owing to the employment of a local co-rotational coordinate system along with a second-order strain-displacement relationship, the neglect of the transverse normal strain, and the decoupled mapping of planar strains and transverse shear strains, as detailed in Ref. [23]. In presenting the results, the various element variants are referred to by acronym keys, as

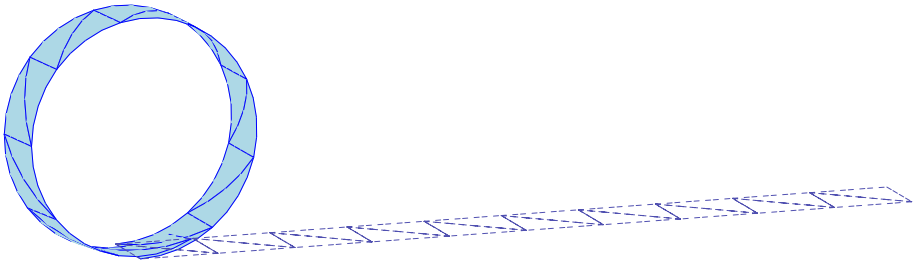

Fig. 31. Deformed configuration of cantilever beam at M_{max}.

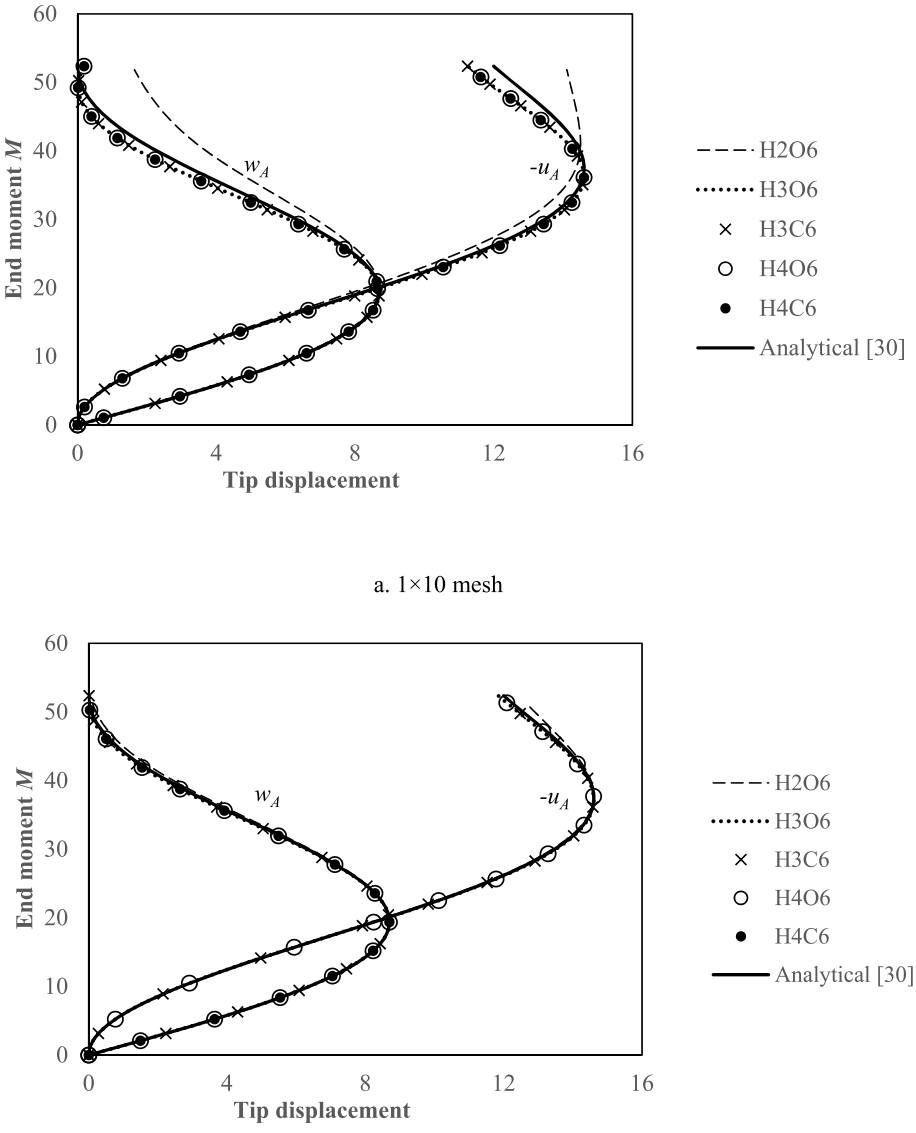

a. 1×10 mesh

b. 2×20 mesh

Fig. 32. Load-displacement curves at cantilever end A with various optimised 6-noded elements.

listed in Table 1.

5.1. Basic element tests

Several basic element tests, including zero energy mode tests, isotropic element tests and constant strain patch tests, have been carried out to study the behaviour of the optimised 6-noded shell elements (H2O6, H3O6, H4O6, H3C6, H4C6) and the MITC6* element.

In the zero energy mode tests, for each of the considered 6-noded element formulations, the stiffness matrix and the corresponding eigenvalues are calculated for a given unrestrained 6-noded shell element, and the number of zero-eigenvalues is counted. As shown in Fig. 5, both regular and irregular triangular element shapes are considered in this test. For all the considered element configurations, both the optimised elements and the mixed element have exactly 6 zero-eigenvalues of the element stiffness matrix, indicating absence of spurious mechanisms.

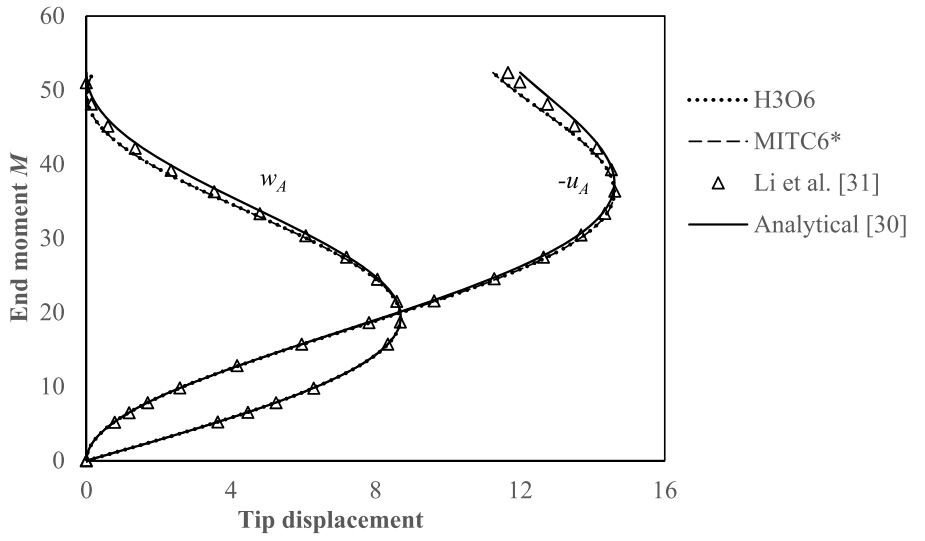

a. 1×10 mesh

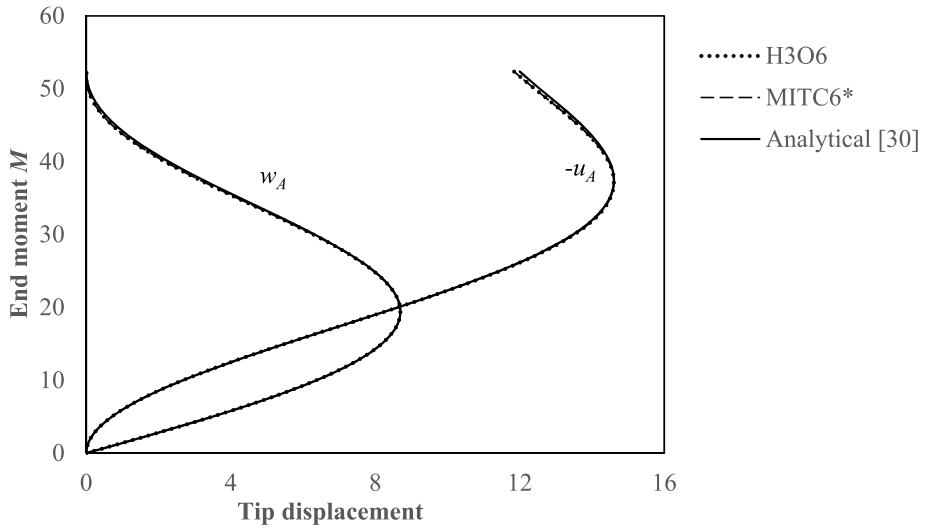

b. 2×20 mesh

Fig. 33. Load-displacement curves at cantilever end A with H3O6 and MITC6* elements.

An arbitrarily shaped triangular element, as depicted in Fig. 6, is employed for the isotropic element test. Geometric and material parameters are given as: thickness $t = 0.001$, Young's modulus $E = 10^6$, and Poisson's ratio $\nu = 0.2$. In this test, 24 sets of strain-inducing displacement modes, as listed in Table 2, are respectively imposed to the optimised and the mixed 6-noded elements. For each prescribed displacement mode, three nodal numbering sequences are used (i.e., 1-2-3-4-5-6, 2-3-1-5-6-4, and 3-1-2-6-4-5, respectively), and the total strain energy by using each nodal ordering is recorded. It is found that for all the optimised and mixed 6-noded elements, the total strain energy for each strain-inducing displacement mode is invariant to nodal ordering, thus indicating that all the considered element types pass the isotropic element test.

Two patches of triangular elements, adapted from a five-quadrilateral-element patch used by MacNeal and Harder [28], are used for constant-strain patch tests, where the first patch consists of elements with straight edges and mid-side nodes (Fig. 7), while the second patch considers a distorted mesh (Fig. 8). Details of the patch tests and the associated results are given in Appendix A. It is observed that all the optimised 6-noded elements pass the test for both the regular and the irregular patch patterns, resulting from the enforcement of zero mean on each hierarchic strain mode. The mixed element MITC6* passes the constant strain patch tests for the regular element mesh only; significant errors are observed in its predictions of strains and displacements for the distorted element mesh.

5.2. *Clamped square plate*

A square plate of dimensions $2L \times 2L \times t$, fully clamped at all four edges, is subjected to a uniformly distributed transverse loading p. The geometric, material, and loading parameters are given as: $L = 1.0$, Young's modulus $E = 1.7472 \times 10^7$, Poisson's ratio $\nu = 0.3$, and $p = 1.0$. The symmetry of the problem allows the modelling of a quarter of the plate with the 6-noded triangular elements, as shown in Fig. 9. The boundary conditions along the clamped edges AB and BC and the edges OA and OC are given as follows: $u = v = w = \theta_x = \theta_y = 0$ along edges AB and BC, $u = \theta_x = 0$ along edge OA, and $v = \theta_y = 0$ along edge OC. The convergence rates of the various 6-noded element types are studied in this linear problem, where the influence of the (t/L) ratio is also investigated.

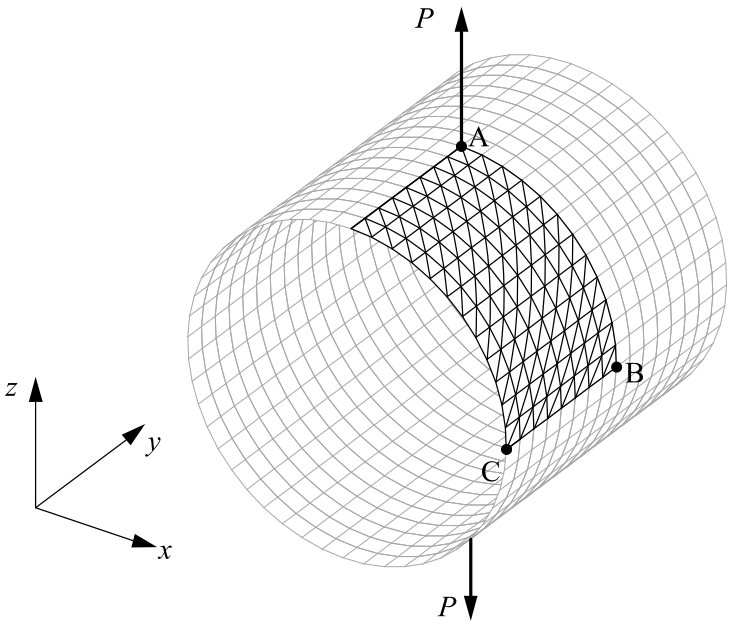

a. Octant model of the cylindrical shell subjected to opposite loads

b. Meshes of 6-noded elements for octant model

Fig. 34. Pull-out of cylindrical shell with free ends.

The convergence curves of the optimised 6-noded elements are compared with the relative error in the strain energy as a measure of accuracy:

$$RE = \frac{|U_{ref} - U|}{U_{ref}} \tag{38}$$

where: U is the total strain energy of a coarse mesh with a nominal element length of h_e; U_{ref} is the reference value, taken as the strain energy obtained from a fine 128 × 128 mesh of the H3O6 element. For $(t/L) = 0.01$, 0.001 and 0.0001, the reference values of U_{ref} are 1.9471 × 10^{-3}, 1.9456 and 1.9456 × 10^{3}, respectively.

Fig. 10 presents the convergence results of various optimised triangular elements, which show a general relief of shear locking for all the considered (t/L) ratios. The H2O6 element, which uses optimisation without hierarchic terms, is not as effective as those with hierarchic corrections in remedying shear locking. Besides, the objective alternative approach, using 3rd or 4th order hierarchic optimisation, is more accurate than the corrective alternative, evident from the higher convergence rates and the lower levels of relative error associated with the H3O6 and H4O6 results in comparison with the H3C6 and H4C6 results. Note that in the case where $(t/L) = 0.01$, the H4O6 and the H4C6 results show a lifted tail after reaching a relatively high accuracy level, which can be due to round-off errors and the relative error measure employed.

In Fig. 11, the results of the H3O6 element are also compared to those of the MITC6* and the MITC6 [19] elements. It is worth noting that the MITC6 [19] results employ the s-norm as a measure of accuracy, given as:

$$RE = \frac{\left\|\mathbf{u}_{ref} - \mathbf{u}_h\right\|_s^2}{\left\|\mathbf{u}_{ref}\right\|_s^2} \tag{39}$$

where: $\mathbf{u}_{ref}$ is the vector of reference nodal displacement values; $\mathbf{u}_h$ is the finite element solution of nodal displacements; $\|\cdot\|_s^2$ is the s-norm.

Although Eqs (38) and (39) do not yield equivalence for non-conforming formulations, it is still reasonable to compare the results of the MITC6 element using the measure of Eq. (39) against the results of the other elements using the measure of Eq. (38). Fig. 11 shows that the H3O6 results have better accuracy and convergence rate than the MITC6

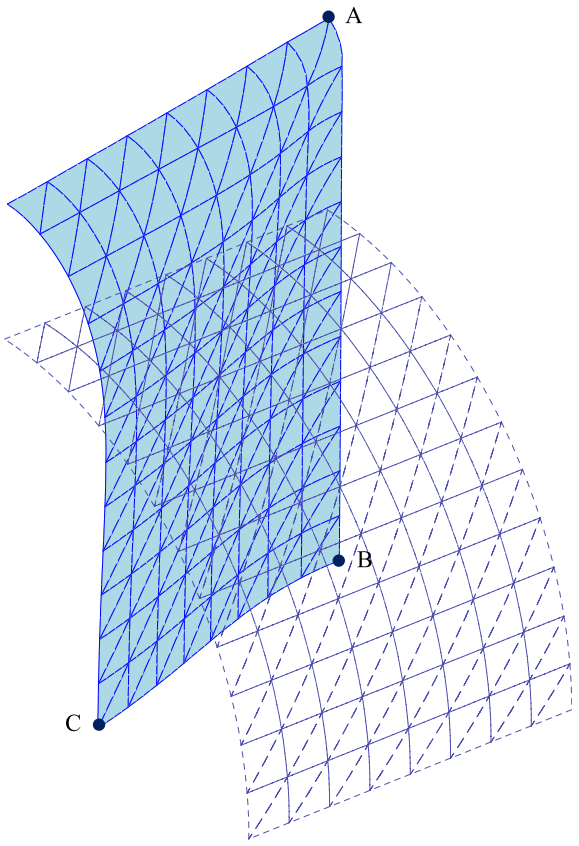

Fig. 35. Deformed configuration of octant cylindrical shell model at $P = 40 \times 10^3$.

results, although there is a noticeable shift of curves upward as (t/L) decreases. It is also shown that the convergence rate of the MITC6* solution is much slower for this problem. The small differences between the MITC6* and the MITC6 results may be due to round-off errors, different accuracy measurement and the formulation differences.

5.3. Cylindrical shell

This is another linear elastic benchmark problem for investigating the performance of the developed 6-noded shell elements. The cylindrical shell depicted in Fig. 12 has a length of $2L$, a radius of R, and a constant thickness t, and is loaded with a periodic pressure $p(\theta) = p_0 \cos(2\theta)$. The geometric and material properties are given as: $L = R = 1.0$, $E = 2.0 \times 10^5$ and $\nu = 1/3$. The amplitude of the pressure is $p_0 = 1.0$. Two boundary conditions at both curved ends are considered: a free boundary condition corresponding to a bending-dominant problem, and a fully clamped boundary condition corresponding to a membrane-dominant problem. Due to symmetry, an octant of the model is analysed with a uniform mesh pattern, as shown in Fig. 12.

The convergence curves of the optimised 6-noded elements are compared, with the relative error in the strain energy as a measure of accuracy, as shown in Eq. (38). The strain energy obtained from a fine 96×96 mesh of the H3O6 element is used as the reference strain energy U_{ref}. For the case where the cylindrical shell has free ends, the reference values of U_{ref} are 2.3480, 2.3337×10^3 and 2.3292×10^6, respectively for (t/L) ratios of 0.01, 0.001 and 0.0001; on the other hand, for the case where the cylindrical shell is clamped at both ends, the reference values of U_{ref} are 8.9607×10^{-4}, 9.3217×10^{-3} and 9.3954×10^{-2}, respectively, for (t/L) ratios of 0.01, 0.001 and 0.0001.

Employing Eq. (38) as the relative error measure, the convergence performances of various optimised 6-noded elements with free and clamped boundary conditions are shown in Figs. 13 and 14, respectively. Significant locking is observed in the H2O6 solution, in particular for the free edge boundary condition, while the other optimised elements exhibit good accuracy and convergence rate, with the H3O6 solution providing slightly better accuracy. In Figs. 15 and 16, the H3O6 results are compared against the MITC6* results; where the MITC6 solution [19] in accordance with the relative error measure of Eq. (39) is also presented for comparison. It is observed that the H3O6 and MITC6* elements have marginally comparable accuracy and convergence rates for the considered boundary conditions and (t/L) ratios. The figures also show that the MITC6 element has slower convergence rates and is less accurate for thin shells $(t/L = 0.0001)$.

5.4. Pinched cylinder

In this linear problem, a cylindrical shell, supported by rigid diaphragms at both ends, is subjected to a pair of pinching loads, as depicted in Fig. 17. The geometric and material properties are given as: $L/R = 2$, $R/t = 100$, $t = 0.01$, $E = 3.0 \times 10^8$, and $\nu = 0.3$. Each pinching load is $P = 300$. Due to symmetry, an octant model of the cylindrical shell is considered with three uniform meshes (4×4, 8×8, and 12×12) of various 6-noded elements, with an 8×8 mesh depicted in Fig. 17. The non-dimensional deflection at the point of loading $\overline{w}_C = w_C Et/P$, is predicted by each of the numerical models. The predictions of $\overline{w}_C$ with various 6-noded shell elements, normalised by the reference value of $\overline{w}_{C,ref} = -164.24$, a series solution obtained by Lindberg et al. [29], are listed in Table 3. Also provided are the normalised results by Bucalem et al. [20], where M6-3 and M7-3 correspond to respectively a 6-noded and a 7-noded triangular element employing an assumed strain method. The poor predictions given by the conforming meshes indicate significant locking. The accuracy of the H3O6 and H4O6 is manifested in a very coarse mesh, followed by the H3C6, H4C6, and M6-3 elements. Although M7-3 provides a prediction closer to 1.0 in the coarse 4×4 mesh, its prediction improves slower than the other elements, evident from persistence of the over-estimation even in a fine mesh of 12×12 elements.

5.5. Hemispherical shell with an 18° cut-out

Another linear problem is used to assess the performance of the proposed quadratic triangular elements. The hemispherical shell depicted in Fig. 18 has an 18° cut-out on its top and is subjected to an orthogonal set of two inward and two outward forces, $2P$. The loading and geometric and material parameters are given as follows: $P = 1.0$, $R = 1.0$, $t = 0.004$, $E = 6.825 \times 10^8$ and $\nu = 0.3$. Due to symmetry, a quarter of the hemispherical shell is modelled with three uniform meshes (4×4, 8×8, and 12×12), and the predictions of the radial deflection at the point of loading (Point A) are compared for the various elements. The displacement predictions by different elements, normalised by the reference value of 0.09355 [20], are listed in Table 4. The results with M6-3 and M7-3 by Bucalem et al. [20] are also presented for comparison. Again, the H4O6 and H3O6 elements provide better accuracy with coarser meshes, followed by their corrective counterparts. More distorted meshes, as shown in Fig. 19 for an 8×8 mesh, are also used to investigate the performance of various elements in overcoming distortion locking, where the three nodes (C, D, E) in a regular mesh are moved to positions (C', D', E'). The accuracy of all element types degrades significantly for a 4×4 mesh owing to the highly distorted element shapes. However, it is observed that an 8×8 mesh of the optimised elements, in particular H3O6 and H4O6, becomes capable of providing good accuracy, while a 16×16 mesh of the MITC6* is required for comparable accuracy.

5.6. Annular plate

This is a large displacement problem where an annular plate is fully

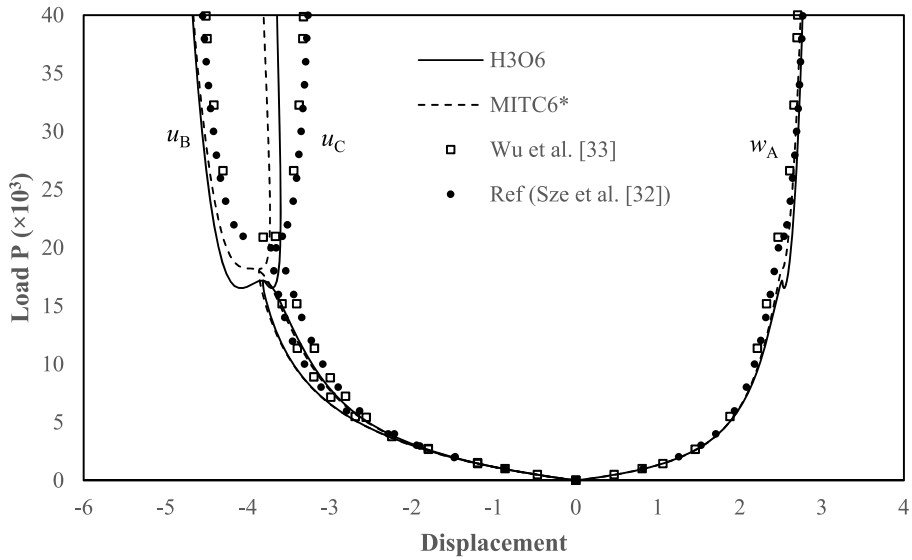

a. 4×6 mesh

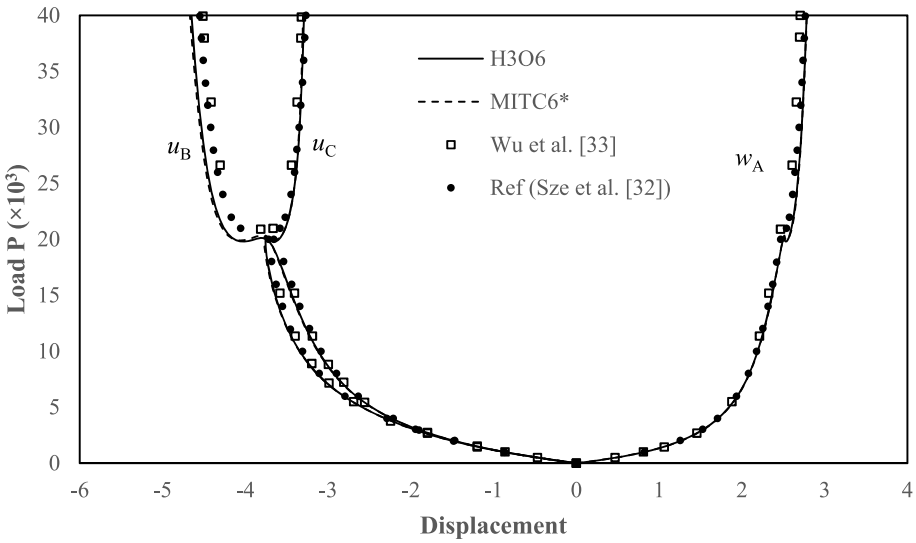

b. 8×12 mesh

Fig. 36. Load-displacement curves of cylindrical shell model with different meshes of H3O6 and MITC6* elements.

clamped at one end and subjected to a uniform transverse loading q at the other end, as shown in Fig. 20. The geometric and material properties are specified as: $R_1 = 6$, $R_2 = 10$, $t = 0.03$, $E = 21.0 \times 10^7$, and $\nu = 0.0$. The plate is modelled with two meshes of the triangular elements (16×1 and 32×2), with the 32×2 mesh depicted in Fig. 20. Fig. 21 shows the final deformed configuration of the plate. The load-vertical deflection response at Points *A*, *B*, and *C* with different meshes and different element types is investigated.

Figs. 22–24 depict the load-displacement curves at points *A*, *B*, and *C* with the H3O6 and the MITC6* elements, and a convergent solution of the H3O6 using a 64×8 mesh is taken as a reference solution. Also plotted are the results by Campello et al. [16], who employed the same meshes with 6-noded triangular elements that are based on the enhanced displacement method. It is observed that the results with the H3O6 element are much closer to the reference solution and notably in the coarser mesh. As the mesh is refined, the performance of the MITC6* element becomes almost comparable to the H3O6 element due to the decreased degree of element irregularity. Fig. 25 also compares the load-deflection curves at point A with the various optimised 6-noded elements for a 16×1 mesh. Again, the optimisation approach with an objective alternative is more accurate than the corrective alternative. Although the H4O6 element yields comparably accurate results with the H3O6 element, H3O6 is preferred due to the fewer integration points required compared to H4O6.

5.7. Pinched hemispherical shell

Fig. 26 depicts a hemispherical shell subjected to two inward and two outward forces 90° apart at its base. The shell is made of an isotropic material with material properties of $E = 6.825 \times 10^7$ and $\nu = 0.3$. The geometric parameters of the hemispherical shell are radius $R = 10.0$ and thickness $t = 0.04$. The variation of radial displacements at Points *A* and

B with the point load P is investigated. A quarter-model is employed due to symmetry, and two alternative meshes of 6-noded elements are employed in the model (each of the three subdomains in the quarter model is discretised into 3×3 and 6×6 mesh patterns, respectively). The results by Arciniega and Reddy [30] are used as a reference solution, which are obtained by a 2×2 mesh of 8th-order tensor-based 81-noded elements (Q81) using first-order shear deformation theory. The final deformed configuration of the pinched hemisphere is depicted in Fig. 27.

The results using optimised 6-noded elements are shown in Fig. 28 for the two meshes. The conforming element CNF6 exhibits considerable inaccuracy, persisting even in the finer mesh, which is mainly attributed to membrane locking. As stated before, the H3O6 and H4O6 elements exhibit superior performance to their corrective counterparts in the coarser mesh, and the discrepancy reduces with mesh refinement. In Fig. 29, the H3O6 results are compared against the MITC6* solution, which again indicates the effectiveness of the H3O6 element in addressing locking notably for the coarser mesh.

5.8. Cantilever beam under end moment

Fig. 30 depicts a thin cantilever beam subjected to an end moment M. The beam is made of an isotropic material with material properties of $E = 1.2 \times 10^6$ and $\nu = 0.0$. The geometric parameters of the cantilever beam are: length $L = 12.0$, width $b = 1.0$ and thickness $t = 0.1$. The variation of vertical and horizontal displacements at the free beam end (w_A and u_A) with the end moment M is investigated. Two alternative meshes of 6-noded elements (1×10 and 2×20) are employed, with the results compared with the reference analytical solution based on the moment-curvature relationship, which is given as follows [30]:

$$\frac{u_A}{L} = \frac{k}{M}\sin\left(\frac{M}{k}\right) - 1, \quad \frac{w_A}{L} = \frac{k}{M}\left(1 - \cos\left(\frac{M}{k}\right)\right)$$

where $k = \frac{EI}{L}$ with $I = \frac{bt^3}{12}$.

Accordingly, the cantilever beam will roll up to a complete circle at an end moment of $M_{max} = 2\pi k = 52.360$. The final deformed configuration of the cantilever beam under bending for a 1×10 mesh of H3O6 elements is depicted in Fig. 31.

Fig. 32 depicts the load-displacement curves using different optimised element variants, all of which show good agreement with the analytical solution, although the H2O6 element exhibits less accuracy for the coarser 1×10 mesh. In Fig. 33, the H3O6 and MITC6* results are compared against the analytical solution. It is observed that both elements perform comparably well even for a coarser 1×10 mesh. Also shown in Fig. 31 a are the results by a 1×20 mesh of 8-noded quadrilateral solid-shell elements (US-ATFHS8) developed by Li et al. [31], which employs an equivalent number of nodal DOFs along the beam length direction as the 1×10 mesh of 6-noded triangular elements. The results show that H3O6 and MITC6* triangular elements yield a comparable capability of addressing locking compared to the quadrilateral elements, with the latter showing a slightly improved accuracy at very large deformations with the use of a smaller element size.

5.9. Pull-out of a cylindrical shell

As depicted in Fig. 34, a cylindrical shell with free ends is subjected to two opposite loads P. The material and geometric properties are as follows: Young's modulus $E = 10.5 \times 10^6$, Poisson's ratio $\nu = 0.3125$, length $L = 10.35$, radius $R = 4.953$ and thickness $t = 0.094$. Due to symmetry, an octant of the shell is modelled using two meshes (4×6 and 8×12) of H3O6 and MITC6*, as illustrated in Fig. 34 b. The variation of vertical displacement at Point A (w_A) and horizontal displacements at Points B and C (u_B and u_C) with the load P is investigated. The converged solution provided by Sze et al. [32] is used as a reference. The deformed configuration of the octant model of 8×12H3O6 elements at $P = 40 \times 10^3$ is shown in Fig. 35.

Fig. 36 depicts the load-displacement curves using H3O6 and MITC6*, which are compared against the reference solution. Also shown in the figure are results given by Wu et al. [33] using an 8×12 mesh of 3-noded triangular flat shell elements (HSDF-PSH3) based on a hybrid stress/displacement formulation. The accuracy of the H3O6 and MITC6* results for the coarser 4×6 mesh reduces to some extent when the cylindrical shell undergoes large deformation, specifically for the horizonal displacements u_B and u_C, while the vertical displacement w_A under the load P, hence the strain energy of the shell, is accurately predicted. This discrepancy at large deformations is mainly attributed to the simplified strain-displacement relationship utilised in the local element formulation, which is based on the assumption of a shallow shell element. At larger loads, some of the elements are excessively deformed with excessive local transverse displacements, which renders the simplified strain-displacement relationship less accurate. Nevertheless, the accuracy of the H3O6 and MITC6* clearly improves with mesh refinement, as demonstrated in Fig. 36 b for the finer 8×12 mesh, which is due to a reduction in the local element transverse displacements and the closer compliance with the shallow shell element assumption.

6. Conclusions

Locking phenomena result from the inability of the element to correctly model lower-order strain modes, depending on the type of structural analysis problem, the underlying assumptions of the associated mathematical model, as well as the element shape and order. This paper proposes variants of 6-noded triangular shell elements based on a recently developed hierarchic optimisation approach, which remedy shear, membrane, and distortion locking by: (i) selecting a set of low-order strain modes in terms of physical coordinates as the objective strain distributions, (ii) enriching the conforming strains with a set of higher-order hierarchic strain modes in terms of natural coordinates, and (iii) minimising the strain errors between the objective and the corrective strains.

In the local formulations of the optimised 6-noded elements, the hierarchic optimisation approach is applied to the membrane, curvature, and transverse shear strains, respectively, for relieving inaccuracies arising from locking phenomena. In order to achieve the desirable characteristic of 'spatial isotropy', the hierarchic optimisation approach is enhanced so that optimisation is applied to the three direct membrane and curvature strains along the edge directions, hence resulting in a local element response that is invariant to nodal ordering. Furthermore, a co-rotational coordinate system is employed for the element variants, which allows large displacement analysis of thin-to-moderately thick plate and shell applications.

Several linear and nonlinear numerical examples have been used to demonstrate the effectiveness of the variants of optimised 6-noded elements in the elimination of locking. Among the optimised elements, the H2O6 element, which employs no hierarchic strain modes in the strain fitting, is still associated with noticeable inaccuracy due to locking, which highlights the importance of the inclusion of the higher-order strain modes for the 6-noded triangular element. For the same hierarchic order, the objective element variant, H*m*O6, yields better accuracy than the corrective alternative, H*m*C6, with the objective alternative based on third order hierarchic optimisation (H3O6) providing the best balance between accuracy and efficiency. The performance of H3O6 is also comparable to the mixed elements based on the MITC6 formulations, and it even shows better accuracy in coarser meshes with irregular element shapes, highlighting its superior ability to relieve distortion locking.

Credit author statement

Y. Liang: Methodology, Writing – original draft, Writing – review & editing, Validation. **B.A. Izzuddin**: Conceptualisation, Methodology, Writing – review & editing, Resources, Supervision.

Declaration of competing interest

The authors declare that they have no known competing financial interests or personal relationships that could have appeared to influence the work reported in this paper.

Appendix A. Constant strain patch tests

A rectangular patch of ten triangular shell elements, adapted from a five-element patch of quadrilateral elements that was suggested by MacNeal and Harder [28], is used herein to examine the membrane and out-of-plane bending behaviour of the optimised and mixed shell elements. As depicted in Fig. 7, the geometric parameters of the patch are given as: length $a = 0.24$, width $b = 0.12$, and thickness $t = 0.001$. The patch is made of an elastic material with Young's modulus $E = 10^6$ and Poisson's ratio $\nu = 0.25$. In this mesh, the edges of each element are straight, and the edge nodes are placed at the centre of each edge. For the membrane patch test, a constant membrane strain state of $\varepsilon_x = \varepsilon_y = \gamma_{xy} = 0.001$ is considered, corresponding to the prescribed edge displacements as follows:

$$u = 10^{-3}\left(x + \frac{1}{2}y\right), \quad v = 10^{-3}\left(y + \frac{1}{2}x\right), \quad w = \theta_x = \theta_y = 0$$

For the out-of-plane bending patch test, a constant bending strain state of $\kappa_x = \kappa_y = \kappa_{xy} = 0.001$ is considered, corresponding to the following prescribed edge displacements:

$$u = v = 0, \quad w = 10^{-3}\frac{(x^2 + xy + y^2)}{2}, \quad \theta_x = 10^{-3}\left(x + \frac{1}{2}y\right), \quad \theta_y = 10^{-3}\left(y + \frac{1}{2}x\right)$$

For both the membrane strain and the out-of-plane bending patch tests, the mesh as shown in Fig. 7 with each of the variants of optimised 6-noded elements and the MITC6* element could accurately predict the displacements and strains at its internal nodes with 0.0% error, hence indicating that all the considered element types pass the patch tests.

The behaviour of the considered 6-noded elements for a more irregular mesh is also investigated, where the original patch is distorted by shifting four edge nodes 13, 14, 15 and 16, either parallel or perpendicular to the edges, and moving the internal node 25 along the x-direction, as illustrated in Fig. 8. All the shifts of nodal positions are of a magnitude d = 0.01. The planar displacements at all internal nodes of the patch, along with planar strains of the two internal elements evaluated at node 25, are compared against the theoretical values. Results of the constant membrane strain patch test using this distorted mesh are listed in Table A.1, which indicate that all the optimised 6-noded elements pass the test owing to the enforcement of zero mean on each hierarchic strain mode. The MITC6*, however, fails in the constant strain patch test for this distorted mesh.

Table A.1
Relative error in transverse and rotational displacements and curvatures in membrane patch test (distorted mesh).

Acronym key	Maximum error in u	Maximum error in v	Maximum error in ε_x	Maximum error in ε_y	Maximum error in γ_{xy}
H2O6	0.0%	0.0%	0.0%	0.0%	0.0%
H3O6	0.0%	0.0%	0.0%	0.0%	0.0%
H4O6	0.0%	0.0%	0.0%	0.0%	0.0%
H3C6	0.0%	0.0%	0.0%	0.0%	0.0%
H4C6	0.0%	0.0%	0.0%	0.0%	0.0%
MITC6*	8.9%	5.6%	18.5%	11.3%	56.1%

References

[1] O.C. Zienkiewicz, R.L. Taylor, J.M. Too, Reduced integration technique in general analysis of plates and shells, Int. J. Numer. Methods Eng. 3 (2) (1971) 275–290.
[2] D.S. Malkus, T.J. Hughes, Mixed finite element methods—reduced and selective integration techniques: a unification of concepts, Comput. Methods Appl. Mech. Eng. 15 (1) (1978) 63–81.
[3] T.J. Hughes, W.K. Liu, Nonlinear finite element analysis of shells: Part I. Three-dimensional shells, Comput. Methods Appl. Mech. Eng. 26 (3) (1981) 331–362.
[4] B.A. Izzuddin, D. Lloyd Smith, Reissner-mindlin plate bending elements with shear freedoms, in: *Proceedings of the 9th International Conference on Civil and Structural Engineering Computing*, 2003. CC2003, The Netherlands.
[5] J.C. Simo, M.S. Rifai, A class of mixed assumed strain methods and the method of incompatible modes, Int. J. Numer. Methods Eng. 29 (8) (1990) 1595–1638.
[6] J. Korelc, P. Wriggers, Improved enhanced strain four-node element with Taylor expansion of the shape functions, Int. J. Numer. Methods Eng. 40 (3) (1997) 407–421.
[7] H.C. Huang, E. Hinton, A nine node Lagrangian Mindlin plate element with enhanced shear interpolation, Eng. Comput. 1 (4) (1984) 369–379.
[8] R.H. MacNeal, Derivation of element stiffness matrices by assumed strain distributions, Nucl. Eng. Des. 70 (1) (1982) 3–12.
[9] K.J. Bathe, E.N. Dvorkin, A formulation of general shell elements—the use of mixed interpolation of tensorial components, Int. J. Numer. Methods Eng. 22 (3) (1986) 697–722.
[10] P.S. Lee, K.J. Bathe, The quadratic MITC plate and MITC shell elements in plate bending, Adv. Eng. Software 41 (5) (2010) 712–728.
[11] P. Panasz, K. Wisniewski, Nine-node shell elements with 6 dofs/node based on two-level approximations. Part I: theory and linear tests, Finite Elem. Anal. Des. 44 (12) (2008) 784–796.
[12] K. Wisniewski, P. Panasz, Two improvements in formulation of nine-node element MITC9, Int. J. Numer. Methods Eng. 93 (6) (2013) 612–634.
[13] B.A. Izzuddin, Y. Liang, A hierarchic optimisation approach towards locking-free shell finite elements, Comput. Struct. 232 (2020) 105839.
[14] J.L. Batoz, K.J. Bathe, L.W. Ho, A study of three-node triangular plate bending elements, Int. J. Numer. Methods Eng. 15 (12) (1980) 1771–1812.
[15] A. Tessler, T.J. Hughes, A three-node Mindlin plate element with improved transverse shear, Comput. Methods Appl. Mech. Eng. 50 (1) (1985) 71–101.
[16] E.M.B. Campello, P.M. Pimenta, P. Wriggers, A triangular finite shell element based on a fully nonlinear shell formulation, Comput. Mech. 31 (6) (2003) 505–518.
[17] J.H. Argyris, M. Papadrakakis, C. Apostolopoulou, S. Koutsourelakis, The TRIC shell element: theoretical and numerical investigation, Comput. Methods Appl. Mech. Eng. 182 (1) (2000) 217–245.
[18] P.S. Lee, K.J. Bathe, Development of MITC isotropic triangular shell finite elements, Comput. Struct. 82 (11) (2004) 945–962.
[19] D.N. Kim, K.J. Bathe, A triangular six-node shell element, Comput. Struct. 87 (23) (2009) 1451–1460.
[20] M.L. Bucalem, S.H.S. da Nóbrega, A mixed formulation for general triangular isoparametric shell elements based on the degenerated solid approach, Comput. Struct. 78 (1) (2000) 35–44.
[21] L.B. da Veiga, D. Chapelle, I.P. Suarez, Towards improving the MITC6 triangular shell element, Comput. Struct. 85 (21) (2007) 1589–1610.
[22] F.G. Flores, E. Onate, Improvements in the membrane behaviour of the three node rotation-free BST shell triangle using an assumed strain approach, Comput. Methods Appl. Mech. Eng. 194 (6–8) (2005) 907–932.

[23] B.A. Izzuddin, Y. Liang, Bisector and zero-macrospin co-rotational systems for shell elements, Int. J. Numer. Methods Eng. 105 (4) (2016) 286–320.
[24] J.C. Simo, F. Armero, R.L. Taylor, Improved versions of assumed enhanced strain tri-linear elements for 3D finite deformation problems, Comput. Methods Appl. Mech. Eng. 110 (3) (1993) 359–386.
[25] J.M. Battini, C. Pacoste, On the choice of local element frame for corotational triangular shell elements, Commun. Numer. Methods Eng. 20 (10) (2004) 819–825.
[26] B.A. Izzuddin, An enhanced co-rotational approach for large displacement analysis of plates, Int. J. Numer. Methods Eng. 64 (10) (2005) 1350–1374.
[27] B.A. Izzuddin, Nonlinear Dynamic Analysis of Framed Structures, PhD Thesis, Imperial College, University of London, 1991.
[28] R.H. MacNeal, R.L. Harder, A proposed standard set of problems to test finite element accuracy, Finite Elem. Anal. Des. 1 (1) (1985) 3–20.
[29] G.M. Lindberg, M.D. Olson, G.R. Cowper, New developments in the finite element analysis of shells, Q. Bull. Division Mech. Eng. Nat. Aeronaut. Establish. 4 (1969) 1–38.
[30] R.A. Acriniega, J.N. Reddy, Tensor-based finite element formulation for geometrically nonlinear analysis of shell structures, Comput. Methods Appl. Mech. Eng. 196 (4) (2007) 1048–1073.
[31] Z. Li, J. Huang, S. Cen, C.F. Li, An unsymmetric 8-node hexahedral solid-shell element with high distortion tolerance: geometric nonlinear formulations, Int. J. Numer. Methods Eng. 120 (5) (2019) 580–606.
[32] K.Y. Sze, X.H. Liu, S.H. Lo, Popular benchmark problems for geometric nonlinear analysis of shells, Finite Elem. Anal. Des. 40 (11) (2004) 1551–1569.
[33] C. Wu, S. Cen, R. Ma, C.F. Li, Shape-free arbitrary polygonal hybrid stress/displacement-function flat shell element for linear and geometrically nonlinear analyses, Int. J. Numer. Methods Eng. 122 (2021) 4172–4218.